A Single-Cell Atlas of Uterine Carcinosarcoma from Diverse Ancestries

Santhilal Subhash[1,2,8], Marie-Thérèse Bammert[1,8], Brian Yueh[1,8], Timothy Chu[3], Mali Barbi[1,4], Aybuke Alici[1], Onur Eskiocak[1,5], Kadir A. Ozler[1], Aaron Nizam[6], Arielle Katcher[6], Charlie Chung[1,5], Vyom Shah[1], Elif Ozcelik[1], Nicolas Robine[3], Marina Frimer[6,7], Gary L. Goldberg[1,6,7], Semir Beyaz[1,*]

[1] Cold Spring Harbor Laboratory, Cold Spring Harbor, NY, USA
[2] Department of Biosciences and Bioengineering, Indian Institute of Technology Jammu, Jammu, India
[3] New York Genome Center, New York, NY, USA
[4] Northwell Health Cancer Institute, New Hyde Park, NY, USA
[5] Graduate Program in Genetics, Stony Brook University, Stony Brook, NY, USA
[6] Division of Gynecologic Oncology, Department of Obstetrics and Gynecology, Northwell Health, Zucker School of Medicine at Hofstra/Northwell, New Hyde Park, NY, USA
[7] Feinstein Institutes for Medical Research, Manhasset, NY, USA
[8] These authors contributed equally

*Correspondence: beyaz@cshl.edu

Abstract

Uterine carcinosarcoma (UCS) is an aggressive endometrial malignancy characterized by epithelial-mesenchymal plasticity, early metastasis, and poor therapeutic response. However, its single-cell organization and microenvironmental interactions remain incompletely defined, particularly in patients of African ancestry who are underrepresented in genomic datasets despite a disproportionate disease burden. Here, we generate a single-cell transcriptomic atlas of UCS from a diverse cohort enriched for patients of African ancestry, integrated with whole-genome sequencing. We identify pronounced inter-patient heterogeneity and resolve epithelial-like, mesenchymal-like, transitional, and stem-like malignant states. Copy-number and trajectory analyses reveal multiple subclones linked along epithelial, progenitor-like, and mesenchymal programs, consistent with metaplastic transitions. Compared to normal endometrium, primary tumors exhibit epithelial-mesenchymal-transition (EMT), mTORC1, and glycolytic programs, whereas metastases show enhanced TNFα-NFκB signaling linked to invasion. The tumor microenvironment comprises diverse immunosuppressive myeloid states and heterogeneous cancer-associated fibroblast populations, including pericyte-like and matrix-remodeling subsets that act as communication hubs via chemokine and immune-checkpoint signaling. These data define the UCS cellular ecosystem in which malignant plasticity is coupled to stromal-immune cell remodeling in a patient cohort of diverse ancestries.

MAIN

Introduction

Uterine carcinosarcoma (UCS) is a rare but highly aggressive subtype of endometrial cancer that accounts for a disproportionate fraction of endometrial cancer-related deaths[1]. Although UCS comprises fewer than 5 % of uterine malignancies, it is associated with high rates of metastasis, recurrence and poor outcomes in advanced stage disease[1–6]. Women of African ancestry face a disproportionate burden, with higher incidence, more aggressive presentation, and lower five-year survival compared with women of European ancestry[7–9]. Despite this disparity, women of African ancestry remain markedly underrepresented in clinical trials and genomic datasets[10–15], leaving critical gaps in our understanding of disease biology and limiting the development of effective, equitable therapeutic strategies.

Histologically, UCS is composed of biphasic malignant epithelial and mesenchymal elements[16]. Genomic studies have strongly supported the view that these components typically share key driver alterations, supporting the view that UCS represents a metaplastic carcinoma rather than a true collision tumor, with phenotypic divergence associated in part with epithelial-mesenchymal transition (EMT)[12,17,18]. Bulk genomic analyses, including TCGA-based studies and subsequent subtype classifications, have identified recurrent alterations in TP53, PI3K-pathway genes, and DNA-repair programs, while implicating EMT-associated transcriptional programs and epigenetic remodeling in sarcomatous differentiation[12,17–20]. However, bulk approaches cannot resolve how malignant cell states along the epithelial-to-mesenchymal continuum relate to clonal architecture or how tumor, stromal, and immune compartments interact to shape UCS ecosystem.

Single-cell approaches offer an opportunity to address these questions in UCS, which exemplifies as a disease of cellular plasticity, histologic admixture, and complex tumor microenvironment[12,17,21,22]. In other gynecologic and solid tumors, single-cell studies have demonstrated that malignant progression is shaped not only by tumor-intrinsic state transitions but also by coordinated programs involving fibroblast, myeloid, and T-cell that collectively create permissive niches for invasion, immune evasion, and therapeutic resistance[23–27]. Whether similar molecular and cellular mechanisms drive UCS remains poorly understood, particularly in patients of African ancestry who have been underrepresented in prior data sets.

To address these gaps, we generated a single-cell atlas of primary and metastatic UCS integrated with matched whole-genome sequencing in an ancestrally diverse cohort enriched for patients of African ancestry. We resolved patient-specific malignant states, clonal architecture, immune phenotypes, and cancer-associated fibroblast (CAFs) programs. Our data provide a valuable resource to identify UCS malignant-stromal-immune cell ecosystem in which epithelial-mesenchymal plasticity is coupled to CAF-associated immune suppression and myeloid recruitment.

Results

An ancestrally diverse single-cell atlas resolves the multicellular architecture of UCS

We profiled 15 UCS specimens from 13 patients, comprising 13 primary tumors and 2 matched metastatic lesions from the ovary and omentum (**Figure 1A**). The cohort was enriched for patients of African ancestry, a population that has been substantially underrepresented in prior UCS studies[12]. Whereas only 16 % of UCS cases in TCGA are from African-ancestry women, 62 % (8/13) of our patients self-identified as African ancestry and comprised diverse demographics for better representation (**Figure 1B**). We performed single-cell RNA sequencing (scRNA-seq) on all 15 tumors and whole-genome sequencing (WGS) on 12 tumors from 10 patients (**Figure 1C-F**). ADMIXTURE[28] analysis of WGS data confirmed that our cohort is enriched for patients of African-ancestry, consistent with self-reported ancestry (**Figure 1C**, **Figure S1A**). MANTIS[29] analysis identified one tumor (CS-014) as microsatellite-instability high (MSI-H), indicative of defective DNA mismatch repair, and associated with a high tumor mutational burden (TMB). Most tumors harbored TP53 alterations, reinforcing its enrichment in aggressive high grade uterine tumors[30,31], together with recurrent mutations in the PI3K signaling pathway (e.g., PIK3CA, PTEN)[12,32,33]. Metastatic samples show overlapping but non-identical mutation patterns compared with primary tumors, indicative of clonal evolution during disease progression.

Across all tumors, we recovered 97,622 high-quality single cells and identified malignant and non-malignant compartments spanning epithelial-like (E-like), mesenchymal-like (M-like), EMT, stem-like/progenitor, stromal, and immune populations (**Figure 1D, E**). Cell type annotation leveraged canonical markers: E-like cells expressed *EPCAM*, *KRT19*, and *FOXJ1*; M-like cells expressed *ENO1*, *IGF2*, *PECAM1*, and *VWF*; stem/progenitor cells expressed *MKI67*, *PRC1*, *CD248*, and *MYC*; EMT cells expressed *CDH11*, *PRRX1*, *SNAI2*, and *ZEB1*; and immune cells expressed *PTPRC*/*CD45* (**Figure S1B**). The relative abundance of these lineages varied dramatically across tumors, highlighting inter-tumoral heterogeneity. Together, this ancestrally diverse single-cell atlas establishes a robust resource for UCS that captures the substantial patient-to-patient variability of malignant composition and tumor microenvironmental architecture.

Copy number analysis reveals highly heterogeneous and plastic cancer cell states in UCS

To distinguish malignant from non-malignant cells while preserving ecosystem context, we inferred RNA-derived copy number alterations using CopyKAT (**Figure S2A**). This resulted in compartmentalization of aneuploid malignant cells from diploid stromal and immune populations, and a small fraction of ambiguous undefined cells, expressing stromal markers (*SPARC*, *MMP2*, *ACTA2*, *ENG*) and immune markers (*PTPRC*, *C1QA*, *IGKC*, *IL2RG*) (**Figure 2A**, **Figure S2A-B**). It revealed that transcriptional heterogeneity was greatest in the cancer compartment, intermediate in stromal cells, and lowest in immune cells (**Figure 2B**, **Figure S2C**). The malignant fraction consisted of E-like, M-like, EMT, and cancer stem cell (CSC) populations (**Figure 2C**), with their relative abundances varying substantially between tumors. Notably, CSC and E-like populations were consistently enriched across UCS samples.

Within the malignant compartment, we identified multiple transcriptionally distinct subtypes. Cancer stem cells (CSCs) segregated into three subtypes: CSC1, CSC2, and CSC3 (**Figure 2C**). CSC1 expressed classical stem-like markers, including *SOX17*, *CLU*, *PAX8*, and *CD24* (**Figure 2D**). Notably, although *SOX17* acts as a tumor suppressor in non-gynecologic cancers, its elevated expression in gynecologic malignancies correlates with aggressiveness and metastatic potential[34], and along with PAX8, reflects Müllerian lineage-specific uterine corpus endometrial carcinoma program[35]. CSC2 exhibited a proliferative, progenitor-like state marked by *CDC20*, *MKI67*, *STMN1*, and *KIAA0101*, a regulator of cancer progenitor growth and invasiveness in multiple tumor types[36,37]. CSC3 expressed mesenchymal stem-like genes, including *VIM* and *SPARC*. All CSC subtypes displayed highly heterogeneous expression patterns across UCS samples.

E-like cells resolved into basal (E1), ciliated (E2), and luminal-like (E3) states, each displaying substantial inter-tumoral variability (**Figure 2C-E**). EMT-like states were highly patient-specific and mostly present in CS-024 and CS-010 (**Figure 2C**, **E**). Together, these findings highlight that UCS cancer cells are profoundly heterogeneous, integrating diverse stem-like, epithelial and mesenchymal programs that are maintained within the tumor ecosystem.

Clonal architectures and transcriptional dynamics reveal tumor-specific evolutionary routes in UCS

Ploidy-informed RNA-derived copy number profiles revealed that each UCS tumor harbors at least two major malignant subclones, which are closely related to each other yet distinct from diploid stromal and immune populations (**Figure 2F-G**). To resolve how these clones relate to cell-state dynamics, we performed RNA velocity and latent-time analyses on the malignant compartment of each tumor. In CS-009, the two primary subclones aligned with transcriptionally distinct trajectories. Clone 1 encompassed E1, CSC3, and CSC2 states, whereas clone 2 was enriched for M1 cells. RNA velocity and latent-time inference indicated a directional flow from early E1 cells through intermediate CSC states toward late M1 cells (**Figure 2H**), recapitulating a metaplastic process consistent with the biphasic epithelial-mesenchymal phenotype characteristics observed in carcinosarcoma[38].

In CS-010, early E2 and M2 states within clone 1 progressed toward CSC and EMT states (**Figure 2I**). Similar patterns were observed in additional UCS tumors (**Figure S2D**), where multiple subclones were anchored by distinct epithelial, progenitor, or mesenchymal programs. Across our patients, these findings support a model in which UCS progression is driven by clonal populations that occupy, and likely traverse, a spectrum of epithelial and mesenchymal identities. The data are therefore most consistent with a metaplastic, state-transition model of UCS biology rather than two independent epithelial and sarcomatous lineages.

Distinct EMT and TNFα-driven programs are revealed in primary and metastatic UCS states

To delineate tumor-specific transcriptional programs, we compared UCS cancer cells with single-cell profiles from normal endometrium obtained from ten donors[39]. Donor cells, derived from women aged 18-34 years, were actively cycling, whereas UCS patients were primarily peri- or post-menopausal (40-88 years). To account for these cell cycle differences, we regressed normal endometrial cells for S- and G2M-phase signatures prior to comparison. This analysis identified 152 genes upregulated and 166 genes downregulated in UCS relative to normal tissue (**Figure 3A**). Primary UCS tumors showed broad upregulation of genes linked to malignant plasticity and stress adaptation, including *CLU*[40], *LCN2*[41], *S100A9*[42], and *VIM*[43]. Pathway analysis identified enrichment of EMT, mTORC1 signaling, glycolysis, hypoxia, and unfolded protein response programs, consistent with a highly adaptive malignant state[44,45]. To investigate potential upstream regulators, we examined enriched transcription factor motifs of differentially expressed genes. This analysis highlighted cyclic-AMP-response element-binding protein (CREB)-associated motifs in upregulated genes (**Figure 3C**).

We next investigated metastatic differences by profiling two metastases (CS-011OM, omentum; CS-011OV, ovary) from the same patient. These metastases displayed distinct transcriptional landscapes and cell-cell communication networks compared with the matched primary tumor (CS-011) (**Figure 3D, Figure S3A**). RNA velocity and latent-time analyses revealed directional trajectories from primary to metastatic tumors, indicating sequential transcriptomic changes during tumor progression (**Figure 3D**). Metastatic lesions exhibited pronounced TNFα-NFκB gene signatures coupled with EMT program engagement compared to the primary tumor (**Figure 3E-G, Figure S3B**), consistent with previous reports that TNFα-driven EMT underlies metastatic competency[46–48].

Together, these analyses suggest that UCS tumors exhibit cellular plasticity that associates with EMT, mTORC1 glycolytic and stress-adaptive programs, with TNFα-NFκB gene signatures coupled to invasive states in metastatic tumors.

Tumor-infiltrating immune cells exhibit high inter-patient heterogeneity in UCS

Given the critical role of the tumor microenvironment in shaping therapeutic response[49,50], and the limited knowledge of immune landscapes in UCS, we profiled tumor-infiltrating immune cells (TIICs) across our cohort. Some of the immune sub-population within TIICs were highly heterogeneous among patients, comprising T-lymphocytes ($CD4^+$, $CD8^+$, and regulatory T-cells/Tregs), B-lymphocytes (B-cells, plasma B cells), myeloid populations (macrophages, monocytes, dendritic cells, mast cells), and innate lymphoid cells (ILCs) (**Figure 4A, S4A–B**).

While some tumors (i.e., CS-005, CS-009, CS-012) were enriched for tumor-associated macrophages (TAMs), others (i.e., CS-007, CS-011) displayed high plasma B-cell infiltration (**Figure 4A**).

By comparison, normal endometrium samples were predominantly enriched for T-lymphocytes, lacking CD4$^+$ T-cells but enriching distinct NK-cell populations, including NKT and double-negative invariant NKT/DNiNKT and contained only macrophages among myeloid cells (**Figure 4B, Figure S4A-B**). Immune profiles in normal tissue were markedly more uniform than in UCS (**Figure S4C**), suggesting a pronounced inter-patient variability of the tumor immune microenvironment. Furthermore, the same TIICs exhibited patient-specific transcriptional programs; for example, CD4$^+$ T-cells expressing *IL7R*, *RORC*, *CCR6*, and *KLRB1* were restricted to certain UCS tumors (CS-005, CS-009, CS-010, CS-011, CS-024), whereas B-lymphocyte and myeloid subsets expressed distinct, tumor-specific markers (**Figure 4C**). Cell scoring revealed selective enrichment of T$_{\text{regs}}$ (*FOXP3*, *IL2RA*) and plasma B cells (*JCHAIN*, *IGHG1-4*, *MZB1*) in specific UCS tumors (**Figure 4D**).

Analysis of cell-cell communication revealed highly variable IL1 signaling during the progression from primary CS-011 to metastatic CS-011OM and CS-011OV (**Figure S4D**). IL1 signaling is known to promote cancer progression and metastasis through myeloid recruitment via *CXCR4* upregulation[51–53], and we observed increased *CXCR4* expression correlating with an increased metastatic phenotype within this patient. These results suggest that UCS tumors may leverage myeloid cell-mediated inflammation to sustain an aggressive microenvironment. Differential gene expression analysis between UCS and normal endometrium further showed transcriptional rewiring in both macrophage and T-cell compartments (**Figure S4E**).

Distinct cytotoxic and immunosuppressive immune states are observed across UCS tumors

Building on the marked inter-patient heterogeneity in TIIC composition, we focused on CD8$^+$ cytotoxic T-cells as central mediators of anti-tumor immunity and key predictors of immunotherapy response[54]. Several UCS tumors exhibited robust CD8$^+$ cytotoxicity accompanied by co-expression of dysfunction/exhaustion (*PDCD1*, *HAVCR2*, *CTLA4*, *PIK3IP1*)[55,56] and cytotoxic markers (*PRF1*, *GZMB*)[57], a phenotype absent in normal endometrium (**Figure 4E-G**).

Notably, CD8$^+$ T-cells from metastatic lesions (CS-011OM, CS-011OV) and one primary tumor (CS-007) contained particularly high cytotoxicity scores, suggesting patient-specific activation of anti-tumor responses.

In parallel, UCS tumors showed a loss of NKT-cell signatures (*CXCL2*, *CD160*, *KLRF1*, *KLRC1*, *KLRB1*, *GNLY*)[58,59] that are abundant in normal endometrium (**Figure 4H**), indicating a shift toward a CD8$^+$-dominated cytotoxic compartment within the tumor microenvironment. Conversely, TAMs displayed an immunosuppressive profile[60], marked by elevated *SPP1*, *CD163*, *FOLR2*, and *GPX1*[61–63](**Figure 4I**). Together, these results show the cellular landscape of UCS immune microenvironment.

UCS stroma is defined by abundant and diverse cancer-associated fibroblast subtypes

Cancer-associated fibroblasts (CAFs) are central stromal components in cancers, including UCS, where they orchestrate extracellular matrix (ECM) remodeling, regulate angiogenesis, and shape immune and metabolic tumor niches[64–66]. To explore the stromal landscape of UCS, we analyzed predicted stromal populations and found that ~71 % of the UCS stromal cells were CAFs, ~23 % were non-CAF populations, including stromal-like, epithelial-like, endothelial, and stem-like cells, and ~6 % formed a mixed cluster expressing stromal, stem, and immune markers (**Figure S5A-B**). CAFs were stringently defined as CD90$^+$/THY1$^+$ fibroblasts lacking immune (PTPRC/CD45$^-$) and endothelial (PECAM1$^-$) signatures in our analysis (**Figure S5B-C**), while non-CAFs contained diverse subpopulations of endothelial, fibroblast, epithelial-like, stem-like, and stromal signatures (**Figure S5D-E**).

CAFs are known to arise from diverse cellular origins, including endothelial cells, resident fibroblasts, epithelial cells, and bone-marrow-derived mesenchymal stem cells[67,68]. Consistent with their multifaceted roles, CD90$^+$/THY1$^+$ CAFs in our dataset segregated into five transcriptionally and functionally distinct subtypes (**Figure 5A-B**): pericyte-like CAFs (periCAFs), FAP$^+$ CAFs, THBS4$^+$ CAFs, antigen-presenting CAFs (apCAFs), and inflammatory CAFs (iCAFs)[69]. Quantification of CAF cell proportions revealed that most UCS tumors exhibited higher proportions of periCAFs and FAP$^+$ CAFs, whereas THBS4$^+$ CAFs, apCAFs, and iCAFs appeared in tumor-specific combinations (**Figure 5C**). In contrast, CAF subtype scoring, reflecting the relative activation of subtype-specific gene expression programs in individual tumors rather than absolute cell abundance, demonstrated consistently high periCAF and apCAF signatures across UCS tumors (**Figure 5D**). Together these analyses suggest that while certain CAF populations may be present at variable frequencies, periCAF and apCAF programs are broadly and transcriptionally active across tumors, in line with their established roles in shaping immune-suppressive microenvironments[70,71]. Notably, multiple CAF subpopulations co-existed within individual tumors, and the defining markers of these subtypes varied across UCS samples, reflecting substantial molecular diversity (**Figure 5E**). For example, iCAFs in CS-019 uniquely expressed *CCL5*, whereas iCAFs in other tumors expressed *CXCR4* (**Figure 5E**).

However, each CAF subtype displayed specialized lineage-specific programs contributing to tumor progression (**Figure 5F**). PeriCAFs expressed pericyte and angiogenic regulators (*RGS5*, *MCAM*, *NOTCH3*), suggesting major roles in vascular remodeling and increased vascular permeability to promote leukocyte infiltration[72–74]. THBS4$^+$ CAFs co-expressed growth factors (*FGFR1*, *SMAD2*, *IGF2*) implicated in tumor expansion across multiple cancers[75–77] together with the lineage-defining marker *THBS4*, a potent ECM activator implicated in tumor expansion across cancers[78,79]. FAP$^+$ CAFs upregulated key ECM regulators (*ELK3*, *CDH11*, *PDGFRA*), consistent with a matrix-modifying role[80–82]. apCAF exhibited robust MHC-II expression, supporting antigen-presenting potential[70,83], while iCAF expressed inflammatory mediators[84] (*IFNG*, *CXCR4*, *CCL2*, *CXCL2*). These chemokines are potent recruiters of leukocytes, including tumor-infiltrating myeloid cells (**Figure S5F**). Collectively, periCAFs and iCAFs expressed chemokine programs predicted to enhance myeloid recruitment, providing a potential link to the myeloid-rich, immune-suppressive microenvironment characteristic for endometrial cancer[85]. These findings indicate that the UCS stromal compartment is not monolithic; instead, it contains multiple specialized fibroblast states with likely non-redundant functions in vascular remodeling, matrix organization, immune regulation, and tumor support.

CAF-directed chemokine and immune checkpoint circuits shape the UCS tumor immune microenvironment (TIME)

To map how stromal-immune interactions reinforce the tumor-supportive niche in UCS, we next mapped ligand-receptor interactions across stromal and immune compartments. This analysis revealed a dense network of CAF-centered signaling involving inflammatory (*IFN*, *IL*, *CCL*, *CXC*), immune checkpoint (*TIGIT*, *CD96*, *PVR*), suppressive (*BTLA*, *OX40*), and anti-tumor (*CD137*) pathways (**Figure 6A**), indicating that stromal-immune crosstalk is a major determinant of UCS immune architecture. We then selected significant cell communications based on patterns with high numbers of signaling genes having high contribution scores (>0.9). Among all cell types, periCAF, FAP$^+$CAF, and CD8$^+$ T cells exhibited the highest global communication activity (**Figure 6B**).

Recent studies highlight chemokine-cytokine networks as key drivers of tumor progression, enabling immune evasion and the recruitment of immunosuppressive populations, including T$_{regs}$, TAMs, tumor-associated neutrophils (TANs), and myeloid-derived suppressor cells (MDSCs)[86]. These recruited leukocytes, particularly macrophages, dampen anti-tumor immunity and reinforce a suppressive microenvironment[87]. In UCS, our stromal analysis revealed that FAP$^+$CAFs prominently express CCL2 (MCP-1) and CXCL2, two chemokines strongly linked to monocyte/macrophage recruitment[88] (**Figure S5F**). TIME-wide ligand-receptor mapping further showed that CCL-CXCL signaling was largely confined to periCAF and FAP$^+$CAF (**Figure 6C**). Through this axis, FAP$^+$CAFs engage both tumor-infiltrating immune cells and cancer cells. The CCL2-CXCL1/2 axis converged with IL10, forming a triad strongly implicated in attracting myeloid cells, including macrophages and TAMs to the tumor bed (**Figure 4I**, **Figure 6D**). This CAF-dominated CCL2-CXCL1/2-IL10 module was also linked to interactions with exhausted CD8$^+$ T cells, suggesting a model in which CAF-derived chemokines actively promote T-cell dysfunction in UCS.

A second dominant signaling module centered on the TIGIT-CD96-PVR immune checkpoint axis (**Figure 6D**), which was highly specific to FAP$^+$CAFs engaging with Tregs and cancer/epithelial cells. Given TIGIT's established role in driving non-cytotoxic and suppressive T-cell states[89], and the emerging involvement of PVR and CD96 in immune evasion[90], this CAF-Treg-tumor triad suggests a stromal route for enforcing immune suppression in UCS. Notably, these signaling circuits varied across tumors (**Figure 6E**). The CCL2-CXCL1/2-IL10 axis was active in CS-005, CS-007, and CS-012, whereas the TIGIT-CD96-PVR module predominated in CS-007, CS-014, and CS-024, highlighting patient-specific immune microenvironmental states.

Together, these findings identify CAFs particularly periCAF and FAP$^+$CAF as important components of the UCS TIME that associate with chemokine-driven myeloid recruitment and immune checkpoint-mediated T-cell suppression. This positions the CCL2-CXCL1/2-IL10 axis and the TIGIT-CD96-PVR axis as promising stromal-targeted entry points for immunotherapeutic intervention in UCS.

Discussion

UCS exemplifies extreme malignant plasticity, immune evasion, and therapeutic resistance, yet its ecosystem-level organization has remained poorly defined[18,91]. Here, we present a comprehensive scRNA-seq and WGS atlas of UCS, enriched for patients of African ancestry, that dissects tumor, stromal, and immune compartments at the level of individual patients. This work establishes a resource and foundation to guide future work. By intentionally avoiding population-level integration, our single cell sample-by-sample strategy preserves patient-specific transcriptional programs, clonal architectures, and signaling states that are otherwise masked in highly plastic malignancies. This approach reveals how tumor-intrinsic diversification is tightly coupled to stromal and immune co-evolution, establishing immunosuppressive, metastasis-prone niches.

Consistent with the biphasic histopathology of UCS[16,38], malignant cells span epithelial, mesenchymal, and EMT-like states that coexist within individual tumors and across genetically distinct clones. Several tumors display dominance of either epithelial-like or mesenchymal-like programs, while others harbor a continuum of states, underscoring pronounced inter- and intra-tumoral heterogeneity. EMT programs are particularly enriched in metastatic tumors and in UCS with high TMB or MSI-H status, supporting lineage plasticity as a key driver of dissemination. Notably, matched primary-to-metastatic analyses of the same patient demonstrate that metastatic competence may encoded early and subsequently refined by microenvironmental selection, refining classical models of UCS histogenesis further[12,18,92]. The shared clonal architecture across epithelial, mesenchymal, and EMT states strongly supports a conversion model, while the early diversification of malignant programs also aligns with aspects of the combination model[12]. In contrast, we find little support for a pure collision model, as biphasic components are not molecularly independent. Together, these findings support a unified view of UCS as a dynamic continuum of malignant states shaped by ecosystem-level pressures.

At the genomic and transcriptional levels, UCS tumors exhibit extensive clonal heterogeneity, with distinct cancer cell subpopulations separated by inferred copy number alterations, transcriptional states, and RNA splicing patterns. The presence of stem-like programs and variable expression of known drivers, such as *SOX17*[34,35,93], further highlights molecular diversification within and between tumors. These findings underscore the need for future whole-genome and functional studies to resolve clonal dependencies for patient-targeted approaches.

The UCS TIME is profoundly reprogrammed and highly heterogeneous across patients. Compared with normal endometrium, UCS tumors exhibit enrichment of immunosuppressive myeloid populations and regulatory T cells, accompanied by loss of NK/NKT cells. Component-resolved analyses show that mesenchymal tumor regions undergo pronounced T-cell exclusion compared to their carcinoma counterparts, highlighting a compartment-specific immune dysfunction that may underpin UCS's poor immunotherapy responsiveness and adverse clinical outcomes[21,92]. CD8$^+$ T cells display variable cytotoxicity and exhaustion states, allowing stratification of UCS tumors into distinct immunological phenotypes ranging from tumor-reactive but dysfunctional to pre-dysfunctional states. This coordinated immune suppression provides mechanistic context for the limited efficacy of PD-1/PD-L1 blockade in UCS[94–96] and emphasizes the importance of identifying alternative immune regulatory axes.

CAFs emerge as dominant organizers of the UCS ecosystem[97]. Multiple CAF states, including inflammatory (iCAFs), antigen-presenting (apCAFs), angiogenic/pericyte-like (periCAF), ECM-remodeling (FAP$^+$ CAFs), and growth factor-secreting (THBS4+ CAFs) populations, coexist within tumors, with periCAFs and FAP$^+$ CAFs frequently acting as signaling hubs. CAF-centered ligand-receptor networks, particularly CCL2-CXCL1/2-IL10 axes, orchestrate myeloid recruitment and T-cell exhaustion, reinforcing immune suppression. In parallel, enrichment of the TIGIT-CD96-PVR immune checkpoint axis highlights tumor-restricted mechanisms of immune evasion and reveals patient-specific vulnerabilities beyond canonical PD-1/PD-L1 signaling.

By integrating ancestrally diverse tumors and resolving patient-specific ecosystem states, this study addresses long-standing gaps in UCS biology and therapeutic equity. While expanded cohorts and mechanistic validation will further refine these insights, our atlas provides a framework for rational combination strategies targeting CAF-driven chemokine signaling, immune reprogramming, and alternative checkpoint pathways. Collectively, UCS progression emerges as a product of co-evolving malignant, stromal, and immune ecosystems, underscoring the need for mechanistically guided, ecosystem-informed interventions in this aggressive and underserved malignancy.

Methods

Description of the Carcinosarcoma cohorts and Ethics statement

This study was approved by the Institutional Review Board at Northwell Health (IRB #18-0897) and Cold Spring Harbor Laboratory (IRB #21-17). All participants provided written informed consent, and all procedures were conducted in accordance with recognized ethical guidelines. Normal endometrium data used was obtained from previously published single cell study by Wang W et al[36]. All UCS patient metadata are summarized in **Table S1** including age, BMI, stage and ethnicity. Sex as a biological variable was not considered because this study is focused on endometrial cancer in female patients. Because sample sizes per ancestry are limited, we do not perform ancestry-stratified statistical comparisons.

P1000 Carcinosarcoma cohort whole genome analysis

DNA extraction and library preparation

DNA was extracted from PBMCs isolated from patient blood or snap frozen tissue using the Zymo Quick-DNA Miniprep kit (Zymo, #D3024) following the manufacturer's instructions. DNA quality and concentration were measured using a Nanodrop ND-1000 Spectrophotometer. Whole genome sequencing (WGS) libraries were prepared using the Truseq DNA PCR-free Library Preparation Kit (Illumina) in accordance with the manufacturer’s instructions. Briefly, 1 ug of DNA was sheared using a Covaris LE220 sonicator (adaptive focused acoustics). DNA fragments underwent bead-based size selection and were subsequently end-repaired, adenylated, and ligated to Illumina sequencing adapters. Final libraries were quantified using the Qubit Fluorometer (Life Technologies) or Spectromax M2 (Molecular Devices) and Fragment Analyzer (Advanced Analytical) or Agilent 2100 BioAnalyzer. Libraries were sequenced on an Illumina Novaseq6000 sequencer using 2x150bp cycles.

Processing and analysis (Alignment, variant calling, Filtering, annotation)

Pre-processing

The New York Genome Center somatic pipeline (v6) was used to process and align the WGS data and call variants. Sequencing reads for the tumor and normal samples are aligned to the reference genome GRCh38 using BWA-MEM (v0.7.15) (arXiv:1303.3997v2 [q-bio.GN]). NYGC’s ShortAlignmentMarking (v2.1) is used to mark short reads as unaligned.

GATK (v4.1.0)[98] FixMateInformation is run to verify and fix mate-pair information, followed by Novosort (v1.03.01) markDuplicates to merge individual lane BAM files into a single BAM file per sample. Duplicates are then sorted and marked, and GATK's base quality score recalibration (BQSR) was performed. The result of the pre-processing pipeline is a coordinate sorted BAM file for each sample.

Quality control

Once preprocessing is complete, we compute several alignment quality metrics such as average coverage, %mapped reads and %duplicate reads using GATK (v4.1.0) and an autocorrelation metric (adapted for WGS from Zang et al.[99]) to check for unevenness of coverage. We also run Conpair[100], a tool developed at NYGC to check the genetic concordance between the normal and the tumor sample and to estimate any inter-individual contamination in the samples.

Variant detection

The tumor and normal bam files are processed through NYGC's variant calling pipeline which consists of MuTect2 (GATK v4.0.5.1)[101], Strelka2 (v2.9.3)[102] and Lancet (v1.0.7)[103] for calling Single Nucleotide Variants (SNVs) and short Insertion-or-Deletion (Indels), SvABA (v0.2.1)[104] for calling Indels and Structural variants (SVs), Manta (v1.4.0)[105] and Lumpy (v0.2.13)[106] for calling SVs and BIC-Seq2 (v0.2.6)[107] for calling Copy-number variants (CNVs). Manta also outputs a candidate set of Indels which is provided as input to Strelka2 (following the developers recommendation, as it improves Strelka2's sensitivity for calling indels >20nt).

Variant merging

Next, the calls are merged by variant type (SNVs, Multi Nucleotide Variants (MNVs), Indels and SVs). MuTect2 and Lancet call MNVs, however Strelka2 does not, and it also does not provide any phasing information. So to merge such variants across callers, we first split the MNVs called by MuTect2 and Lancet to SNVs, and then merge the SNV callsets across the different callers. If the caller support for each SNV in a MNV is the same, we merge them back to MNVs. Otherwise those are represented as individual SNVs in the final callset. Lancet and MantaSV are the only tools that can call deletion-insertion (delins or COMPLEX) events. Other tools may represent the same event as separate yet adjacent indel and/or SNV variants. Such events are relatively less frequent, and difficult to merge. We therefore do not merge COMPLEX calls with SNVs and Indels calls from other callers. The SVs are converted to bedpe format, all SVs below 500bp are excluded and the rest are merged across callers using bedtools[108] pairtopair (slop of 300bp, same strand orientation, and 50% reciprocal overlap).

Somatic variant annotation (SNVs, Indels, CNVs, and SVs)

SNVs and Indels are annotated with Ensembl as well as databases such as COSMIC (v86)[109], 1000Genomes (Phase3)[110], ClinVar (201706)[111], PolyPhen (v2.2.2)[112], SIFT (v5.2.2)[113], FATHMM (v2.1)[114], gnomAD (r2.0.1)[115] and dbSNP (v150)[116] using Variant Effect Predictor (v93.2)[117]. For CNVs, segments with log2 > 0.2 are categorized as amplifications, and segments with log2 < -0.235 are categorized as deletions (corresponding to a single copy change at 30% purity in a diploid genome, or a 15% Variant Allele Fraction). CNVs of size less than 20Mb are denoted as focal and the rest are considered large-scale.

We use bedtools[108] for annotating SVs and CNVs. All predicted CNVs are annotated with germline variants by overlapping with known variants in 1000 Genomes and Database of Genomic Variants (DGV) (22). Cancer-specific annotation includes overlap with genes from Ensembl[118] and Cancer Gene Census in COSMIC, and potential effect on gene structure (e.g. disruptive, intronic, intergenic). If a predicted SV disrupts two genes and strand orientations are compatible, the SV is annotated as a putative gene fusion candidate. Note that we do not check reading frame at this point. Further annotations include sequence features within breakpoint flanking regions, e.g. mappability, simple repeat content and segmental duplications.

Somatic variant filtering

Panel Of Normals

The Panel Of Normals (PON) filtering removes recurrent technical artifacts from the somatic variant callset[101].

PON generation

The Panel of Normals for SNVs, indels and SVs was created with whole-genome sequencing data from normal samples from 242 unrelated individuals. Of these, sequencing data for 148 individuals was obtained from the Illumina Polaris project which was sequenced on the HiSeqX2 platform with PCR-free sample preparation. The remaining samples were sequenced by the NYGC. Of these, 73 individuals were sequenced on HiSeqX, 11 on NovaSeq, and 10 were sequenced on both. We ran MuTect2 in artifact detection mode and Lumpy in single sample mode on these samples.

For SNVs and indels, we created a PON list file with sites that were seen in two or more individuals.

For SVs, we used SURVIVOR (v1.0.3)[119] to merge Lumpy calls. Variants were merged if they were of the same type, had the same strand orientation, and were within 300bp of each other (maximum distance). We did not specify a minimum size. After merging SVs, we used these calls as a PON list.

PON filtering

For SNVs and Indels, we use the PON list to filter the somatic variants in the merged SNV and indel files. To filter our somatic SV callset, we merge our PON list with our callset using bedtools pairtopair (slop of 300bp, same strand orientation, and 50% reciprocal overlap), and filtered those SVs found in two or more individuals in our PON.

Common germline variants

In addition to the PON filtering, we remove SNVs and Indels that have minor allele frequency (MAF) of 1% or higher in either 1000Genomes (phase 3) or gnomAD (r2.0.1)[115], and SVs that overlap DGV and 1000Genomes (phase3). CNVs are annotated with DGV and 1000 Genomes but not filtered.

All Somatic and High-confidence variants

Variants that pass all of the above-mentioned filters are included in our final somatic callset (hereby referred to as AllSomatic). For SNVs, indels and SVs, we also annotate a subset of the somatic callset as high confidence. For SNVs and indels, high confidence calls are defined as those that are either called by two or more variant callers, or called by one caller and also seen in the Lancet validation calls or in the Manta SV calls.

For structural variants, high confidence calls are taken from the somatic callset if they meet the following criteria: called by 2 or more variant callers, or called by Manta or Lumpy with either additional support from nearby CNV changepoint or split-read support from SplazerS[115], an independent tool used to calculate the number of split-reads supporting SV breakpoints. An SV is considered supported by SplazerS if it found at least 3 split-reads in the tumor only. Nearby CNV changepoints are determined by overlapping BIC-Seq2 calls with the SV callset using bedtools closest. An SV is considered to be supported by a CNV changepoint if the breakpoint of the CNV is within 1000bp of an SV breakpoint.

MSI detection

We run MANTIS (v1.0.4)[29] for Microsatellite Instability (MSI) detection in microsatellite loci (found using RepeatFinder, a tool included with MANTIS). A sample is considered to be microsatellite unstable if it's Step-Wise Difference score reported by MANTIS is greater than 0.4 (or 0.62 in absence of a matched-normal). Otherwise, it is considered to be microsatellite stable (MSS).

Genetic ancestry estimation

Ancestry proportion is determined by the software ADMIXTURE[28] v1.3.0, which uses a maximum likelihood-based method to estimate the proportion of reference population ancestries in a sample. We genotyped the reference markers generated from 1,964 unrelated 1000 Genomes project samples directly on the samples using GATK pileup. Individuals from populations MXL (Mexican Ancestry from Los Angeles USA), ACB (African Caribbean in Barbados), and ASW (African Ancestry in Southwest US) were excluded from the reference due to being putatively admixed. The reference was further filtered by using only SNP markers with a minimum minor allele frequency (MAF) of 0.01 overall and 0.05 in at least one 1000 genomes superpopulation. Variants are additionally linkage disequilibrium (LD) pruned using PLINK v1.9 with a window size of 500kb, a step size of 250kb and r2 threshold of 0.2. The analysis results in a proportional breakdown of each sample into 5 continental populations (AFR, AMR, EAS, EUR, SAS) and 23 sub-populations.

Single Cell Profiling by Chromium 10X sequencing and Analysis

Tissue processing, cell preparation, and library construction

Surgical resections of 15 specimens (13 primary and 2 metastasis) from 13 UCS patients were taken and the tissues were dissociated according to Katcher et al.[121,122]. In brief, tissue was washed with cold 1X PBS and minced into small (~0.25 cm) fragments, before being transferred to 5 ml of RPMI media (Sigma Aldrich, #R8758) containing 1 mg/mL Collagenase (Sigma Aldrich, #C9407) and 10 µM Y-27632 dihydrochloride (Tocris, #1254). Tissue suspension was transferred to a rotating incubator (speed: 30 rpm, 37 °C) for 60-120 min depending on successful tissue dissociation. Supernatant was transferred and centrifuged at 300 g for 5 min at room temperature (RT). Supernatant was discarded and the pellet was resuspended in 3 mL of TrpLE Express

Enzyme (1X, no phenol red, Thermo Fisher Scientific, #12604103) with 10 µM Y-27632 dihydrochloride followed by an incubation of 10-20 min at 37 °C with regular mixing. To stop the reacting 3 mL of ADMEM/F12 (Life Technologies, #312634028) was added and the cell suspension centrifuged at 300 g for 5 min at RT. The sample was then filtered through a 40um cell strainer (Corning, #431750) and dead cell removal was conducted using the Dead Cell Removal Kit (Miltenyi Biotec 130-090-101), following the manufacturer's instructions. Samples averaged 80-90% viability with at least 1.5 million cells. Samples are processed for sequencing with Chromium Next GEM Chip G (10x Genomics). GEM generation and barcoding, reverse transcription, cDNA generation and library construction using 3′ Gene Expression Library Construction using the Chromium Single Cell 30 Library (v3 chemistry) following the manufacturer’s protocol. Dual-indexed, single-cell libraries were pooled and sequenced in paired-end reads on Novaseq (Illumina).

Single-cell analysis

Raw reads from FASTQ files are aligned to reference genome GRCh38 and quantified for GRCh38.84 gene annotation using CellRanger (v.6.0.0) (https://10xgenomics.com). First, the CellRanger *mkfastq* command with the CellRanger sample sheet was used to demultiplex the base call files for each flow cell into FASTQ files. Second, the CellRanger *count* command was called to generate single cell feature counts for each library by specifying the library name in the argument. The filtered feature barcode matrix was used for further data analysis.

Quality check and clustering

The downstream analysis using feature barcode matrix was performed using Seurat (v.3.0.0) package. Individual patients with their feature barcode matrix libraries were converted into Seurat object using *Read10X* and *CreateSeuratObject*. For each individual patients we removed cells with high mitochondrial content (>20%) and cells with less than 200 genes. These cut-offs are based on QC inspection and previous single cell studies on endometrium/ovarian[39,123]. Subsequently, the gene in remaining 97,622 cells were log normalized, variable genes detected, scaled and the principal components computed. The top principal components were identified and used for the UMAP and t-SNE dimensionality reduction. Normal endometrium singe cell data from *Wang W et al.*[39], was filtered using the cutoffs mentioned in the publication and the clustering is performed like UCS patients.

Heterogeneity and Assignment of cell types

Initial clustering was performed, and UCS patients showed highly heterogenous profiles. Individual clusters are assigned to a patient based on proportion of cells from the patient contributing to the cluster. Hence the gene markers are predicted per cluster in individual UCS patient by *FindAllMarkers* function from Seurat. This method of assigning gene markers and cell types preserved both molecular and cellular-level heterogeneity in UCS patients. Similar approach was used in prediction of gene markers and cell type assignment for normal endometrium singe cell data from *Wang W et al*.[39] Scoring of cells for different functional modules are done using *AddModuleScore_UCell* function from UCell R package.

RNA abundance-based copy number alteration (rCNA) profiling

Later the cells from UCS patients were subjected to CopyKat analysis with default parameters to determine cancerous and non-cancerous cells in patients' single-cell data by extracting ploidy information by measuring RNA copy number abundance (rCNA) in the genome (https://github.com/navinlabcode/copykat)[124]. The Aneuploid cells were assigned cancerous and remaining diploid cells as non-cancerous. We used hierarchical clustering with Euclidean distance measure to segregate cancerous cells from non-cancerous cells and to determine subclonal profiles within predicted cancer cells. We tested the subclonal profiles using different cutoffs for number of trees (subclusters) and found 2 optimal tree (subcluster) per patient(https://github.com/decodebiology/Carcinosarcoma_singlecell_atlas). We were able to separate non-cancerous diploid cells as immune and non-immune (Stroma) profiles based on the gene markers (**Figure S2B**). The undefined cells by CopyKat express both stroma and immune gene markers and was excluded from further analysis. The individual components such as cancer, immune, and stroma was further analyzed separately. We have performed ligand-receptor interaction analysis to identify cell-cell communications and signaling in the individual components using CellChat[125].

Differential expression analysis

Differential expression (DE) analysis between normal endometrium and UCS predicted cancer cells were performed by implementing Libra using *run_de* function (https://github.com/neurorestore/Libra)[126]. We used single cell appropriate statistical method

Wilcoxon Rank-Sum test to find differentially expressed genes. Similarly, DE analysis was performed between UCS primary and metastatic stages, between normal endometrium immune profile and UCS tumor infiltrating immune profile. Significant DE genes were selected based on adjusted p-value (<0.05) and log-fold-change (±1.0) cutoffs. Obtained DE genes were subjected to functional enrichment analysis with human MSigDB hallmark gene sets (https://gsea-msigdb.org) and gene ontology (https://geneontology.org) using GeneSCF (v1.1-p3) tool[127]. The enriched gene sets are selected by p-value<0.05 cutoff.

Promoter Sequence Based Motif Enrichment Analysis

Using custom scripts we extracted nucleotide sequences (FASTA) from the promoters (± 250 bp from TSS) of list of significantly differentially expressed genes between UCS predicted cancer cells and normal endometrium (https://github.com/decodebiology/extract_promoter_sequence) with GRCh38.84 gene and genome annotation. Obtained FASTA sequences were used to find enriched transcription factor motifs using SEA (v5.5.5) from MEME tool[128]. Motif database HOCOMOCO (v11) full human was used, and the shuffled primary sequences preserving 3-mer frequencies are considered as control sequences. Also, 10% of the input sequences were randomly assigned to the hold-out set to improve p-value accuracy. The motifs are selected based on enrichment E-value of 10 or smaller. Motifs analysis was performed independently on both up and downregulated genes.

Cell-Cell Communication Analysis by Ligand-receptor Interactions

We have performed ligand-receptor interaction analysis to identify cell-cell communications between three components of UCS tumors such as cancer-immune-stroma/CAF using CellChat[125]. From the analysis we obtained multiple patterns of interaction profiles between cell types and individual patterns are clustered based on the interaction strength between cell types. We selected significant cell communications based on patterns with a greater number of cell types interacting with high contribution score (>0.9). Signaling (ligand-receptor interactions) that are contributing to this cell-cell communications between these cell types are extracted for further analysis. Cell types having higher activity was assigned using incoming and outgoing signal strengths. We looked for other cell types that are interacting with highly active cell types with the corresponding signaling contributions resulting in interactions. These signaling genes were then subjected to StringDB to find coregulation patterns among them.

Data and Code Availability

The genomic sequencing data will be deposited in dbGAP repository with accession and the single cell RNA-seq dataset will be accessed from GEO repository upon acceptance of the manuscript.

Acknowledgements

We thank the members of the Beyaz lab for critical discussions. We thank Northwell Health Biospecimen Repository and the Gynecologic Oncology staff for assistance in recruitment of patients from diverse demographics and acquisition of specimens for this study. We thank Cold Spring Harbor Laboratory Cancer Center Shared Resources (Flow Cytometry, Microscopy, Sequencing, Organoid and Histology Core Facilities) supported in part by the National Cancer Institute Cancer Center Support Grant (5P30CA045508). This work was financially supported by grants to S.B from the National Cancer Institute (R37CA292807), Oliver S. and Jennie R. Donaldson Charitable Trust, the Mark Foundation for Cancer Research (20-028-EDV), the Cold Spring Harbor Laboratory and Northwell Health Affiliation, New York Genome Center Polyethnic-1000 Initiative. The sample processing, computations, and depositions of the datasets from this study and TCGA was performed on High Performance Computing (HPC) resources Elzar and Agastya provided by Cold Spring Harbor Laboratory and Indian Institute of Technology Jammu respectively.

References

1. Bogani, G. *et al.* Endometrial carcinosarcoma. *Int. J. Gynecol. Cancer* **33**, 147–174 (2023).
2. Artioli, G. *et al.* Rare uterine cancer: Carcinosarcomas. Review from histology to treatment. *Crit. Rev. Oncol. Hematol.* **94**, 98–104 (2015).
3. Matsuo, K. *et al.* Significance of Lymphovascular Space Invasion by the Sarcomatous Component in Uterine Carcinosarcoma. *Ann. Surg. Oncol.* **25**, 2756–2766 (2018).
4. Pham, E. N. B. *et al.* Quality of life and survival in patients with uterine carcinosarcoma: A tertiary center observational study. *Gynecol. Oncol. Rep.* **57**, 101679 (2025).
5. Novin, K., Shahrokh, S., Shahin, M. & Taghizadeh-Hesary, F. Long-Term Complete Remission of Metastatic Endometrial Carcinosarcoma With Radical Surgical Resection and Postoperative Chemotherapy Utilizing Paclitaxel and Carboplatin. *Cancer Rep.* **8**, e70346 (2025).
6. Sağnıç, S. *et al.* Uterine Carcinosarcoma: Adaptation to New FIGO 2023 Staging System Through Clinical Profile and Oncologic Outcomes. *J. Clin. Med.* **14**, (2025).
7. Saris, D. H. *et al.* Disparities in cancer-specific and overall survival in black women with endometrial cancer: A Medicare-SEER study. *Gynecol. Oncol. Rep.* **40**, 100922 (2022).
8. Doll, K. M. & Winn, A. N. Assessing endometrial cancer risk among US women: long-term trends using hysterectomy-adjusted analysis. *Am. J. Obstet. Gynecol.* **221**, 318.e1-318.e9 (2019).
9. Mukerji, B. *et al.* Racial disparities in young women with endometrial cancer. *Gynecol. Oncol.* **148**, 527–534 (2018).
10. Illah, O., Adeeko, D., Olaitan, A. & Gentry-Maharaj, A. Racioethnic Disparities in Endometrial Cancer Outcomes. *Diagn. Basel Switz.* **14**, (2024).

11. Wolf, J. L., Hamilton, A., An, A., Leonard, J. P. & Kanis, M. J. Racial Disparities in Endometrial Cancer Clinical Trial Representation: Exploring the Role of Eligibility Criteria. *Am. J. Clin. Oncol.* **47**, (2024).

12. Cherniack, A. D. *et al.* Integrated Molecular Characterization of Uterine Carcinosarcoma. *Cancer Cell* **31**, 411–423 (2017).

13. Kandoth, C. *et al.* Integrated genomic characterization of endometrial carcinoma. *Nature* **497**, 67–73 (2013).

14. Darko, N., Millet, N., Usman, A., Teece, L. & Moss, E. L. Exploring the perspectives of underrepresented voices: Perceptions and experiences of uterine cancer for black African, Caribbean, black British, and mixed-black women in the UK to develop strategies for early symptom presentation. *Gynecol. Oncol.* **180**, 132–138 (2024).

15. Montes de Oca, M. K. *et al.* Diversity and transparency in gynecologic oncology clinical trials. *Cancer Causes Control* **34**, 133–140 (2023).

16. Liu, Y. *et al.* Assessing inter-component heterogeneity of biphasic uterine carcinosarcomas. *Gynecol. Oncol.* **151**, 243–249 (2018).

17. Gotoh, O. *et al.* Clinically relevant molecular subtypes and genomic alteration-independent differentiation in gynecologic carcinosarcoma. *Nat. Commun.* **10**, 4965 (2019).

18. Gopinatha Pillai, M. S. *et al.* Uterine carcinosarcoma: Unraveling the role of epithelial-to-mesenchymal transition in progression and therapeutic potential. *FASEB J.* **38**, e70132 (2024).

19. Li, J. *et al.* Whole-Genome DNA Methylation Profiling Identifies Epigenetic Signatures of Uterine Carcinosarcoma. *Neoplasia N. Y. N* **19**, 100–111 (2017).

20. Zhang, N. *et al.* Epigenetic Signatures and Prognostic Biomarkers Analysis of Methylation-Driven Genes in Uterine Endometrial Carcinosarcoma. *Crit. Rev. Eukaryot. Gene Expr.* **35**, 27–47 (2025).

21. Garg, V. *et al.* Elucidating divergent biology in uterine carcinosarcoma. *Transl. Oncol.* **61**, 102506 (2025).

22. Nakad Borrego, S., Lengyel, E. & Kurnit, K. C. Molecular Characterizations of Gynecologic Carcinosarcomas: A Focus on the Immune Microenvironment. *Cancers* **14**, (2022).

23. Puram, S. V. *et al.* Single-Cell Transcriptomic Analysis of Primary and Metastatic Tumor Ecosystems in Head and Neck Cancer. *Cell* **171**, 1611-1624.e24 (2017).

24. Luo, H. *et al.* Pan-cancer single-cell analysis reveals the heterogeneity and plasticity of cancer-associated fibroblasts in the tumor microenvironment. *Nat. Commun.* **13**, 6619 (2022).

25. Izar, B. *et al.* A single-cell landscape of high-grade serous ovarian cancer. *Nat. Med.* **26**, 1271–1279 (2020).

26. Imianowski, C. J., Chen, Q., Workman, C. J. & Vignali, D. A. A. Regulatory T cells in the tumour microenvironment. *Nat. Rev. Cancer* **25**, 703–722 (2025).

27. Miller, T. E. *et al.* Programs, origins and immunomodulatory functions of myeloid cells in glioma. *Nature* **640**, 1072–1082 (2025).

28. Alexander, D. H., Novembre, J. & Lange, K. Fast model-based estimation of ancestry in unrelated individuals. *Genome Res.* **19**, 1655–1664 (2009).

29. Kautto, E. A. *et al.* Performance evaluation for rapid detection of pan-cancer microsatellite instability with MANTIS. *Oncotarget* **8**, 7452–7463 (2017).

30. Moretti, N. R. *et al.* Impact of TP53 somatic mutations on prognosis in endometrial cancer: a systematic review and meta-analysis. *Clin. Transl. Oncol. Off. Publ. Fed. Span. Oncol. Soc. Natl. Cancer Inst. Mex.* https://doi.org/10.1007/s12094-025-04076-9 (2025) doi:10.1007/s12094-025-04076-9.

31. Pham, E. N. B. *et al.* Molecular diversity in uterine carcinosarcoma: Beyond TP53. *Gynecol. Oncol.* **198**, 75–83 (2025).

32. Hong, B., Le Gallo, M. & Bell, D. W. The mutational landscape of endometrial cancer. *Curr. Opin. Genet. Dev.* **30**, 25–31 (2015).

33. Oda, K., Stokoe, D., Taketani, Y. & McCormick, F. High frequency of coexistent mutations of PIK3CA and PTEN genes in endometrial carcinoma. *Cancer Res.* **65**, 10669–10673 (2005).

34. Satturwar, S. *et al.* SOX17 is a highly sensitive and specific marker for metastatic ovarian and endometrial carcinomas in cytology cell block specimens. *Cancer Cytopathol.* **131**, 465–470 (2023).

35. Lin, L. *et al.* SOX17 and PAX8 constitute an actionable lineage-survival transcriptional complex in ovarian cancer. *Oncogene* **41**, 1767–1779 (2022).

36. Jain, M., Zhang, L., Patterson, E. E. & Kebebew, E. KIAA0101 is overexpressed, and promotes growth and invasion in adrenal cancer. *PloS One* **6**, e26866 (2011).

37. Kais, Z. *et al.* KIAA0101 interacts with BRCA1 and regulates centrosome number. *Mol. Cancer Res. MCR* **9**, 1091–1099 (2011).

38. McConechy, M. K. *et al.* In-depth molecular profiling of the biphasic components of uterine carcinosarcomas. *J. Pathol. Clin. Res.* **1**, 173–185 (2015).

39. Wang, W. *et al.* Single-cell transcriptomic atlas of the human endometrium during the menstrual cycle. *Nat. Med.* **26**, 1644–1653 (2020).

40. Fu, Y., Du, Q., Cui, T., Lu, Y. & Niu, G. A pan-cancer analysis reveals role of clusterin (CLU) in carcinogenesis and prognosis of human tumors. *Front. Genet.* **13**, 1056184 (2022).

41. Huang, B. *et al.* Oncogenic and tumor-suppressive roles of Lipocalin 2 (LCN2) in tumor progression. *Oncol. Res.* **33**, 567–575 (2025).

42. Chen, Y., Wu, Z. & Yi, X. Elucidating the pan-oncologic landscape of S100A9: prognostic and therapeutic corollaries from an integrative bioinformatics and Mendelian randomization analysis. *Sci. Rep.* **14**, 19071 (2024).

43. Liu, S. *et al.* High Vimentin Expression Associated with Lymph Node Metastasis and Predicated a Poor Prognosis in Oral Squamous Cell Carcinoma. *Sci. Rep.* **6**, 38834 (2016).

44. Mafi, S. *et al.* mTOR-Mediated Regulation of Immune Responses in Cancer and Tumor Microenvironment. *Front. Immunol.* **12**, 774103 (2021).

45. Gulhati, P. *et al.* mTORC1 and mTORC2 Regulate EMT, Motility, and Metastasis of Colorectal Cancer via RhoA and Rac1 Signaling Pathways. *Cancer Res.* **71**, 3246–3256 (2011).

46. Shi, G. *et al.* Kanglaite inhibits EMT caused by TNF-α via NF-κB inhibition in colorectal cancer cells. *Oncotarget* **9**, 6771–6779 (2018).

47. Wang, H. *et al.* Epithelial-mesenchymal transition (EMT) induced by TNF-α requires AKT/GSK-3β-mediated stabilization of snail in colorectal cancer. *PloS One* **8**, e56664 (2013).

48. Tan, W. *et al.* TNF-α is a potential therapeutic target to overcome sorafenib resistance in hepatocellular carcinoma. *EBioMedicine* **40**, 446–456 (2019).

49. Grant, G. & Ferrer, C. M. The role of the immune tumor microenvironment in shaping metastatic dissemination, dormancy, and outgrowth. *Trends Cell Biol.* https://doi.org/10.1016/j.tcb.2025.05.006 doi:10.1016/j.tcb.2025.05.006.

50. Desai, S. A., Patel, V. P., Bhosle, K. P., Nagare, S. D. & Thombare, K. C. The tumor microenvironment: shaping cancer progression and treatment response. *J. Chemother. Florence Italy* **37**, 15–44 (2025).

51. Sun, Y. *et al.* Pro-Inflammatory Cytokine IL-1β Up-Regulates CXC Chemokine Receptor 4 via Notch and ERK Signaling Pathways in Tongue Squamous Cell Carcinoma. *PloS One* **10**, e0132677 (2015).

52. Tulotta, C. *et al.* CXCR4 signaling regulates metastatic onset by controlling neutrophil motility and response to malignant cells. *Sci. Rep.* **9**, 2399 (2019).

53. Deng, J. & Fleming, J. B. Inflammation and Myeloid Cells in Cancer Progression and Metastasis. *Front. Cell Dev. Biol.* **9**, 759691 (2021).

54. Raskov, H., Orhan, A., Christensen, J. P. & Gögenur, I. Cytotoxic CD8(+) T cells in cancer and cancer immunotherapy. *Br. J. Cancer* **124**, 359–367 (2021).

55. Tietscher, S. *et al.* A comprehensive single-cell map of T cell exhaustion-associated immune environments in human breast cancer. *Nat. Commun.* **14**, 98 (2023).

56. Corselli, M. *et al.* Single cell multiomic analysis of T cell exhaustion in vitro. *Cytometry A* **101**, 27–44 (2022).

57. Oh, D. Y. & Fong, L. Cytotoxic CD4+ T cells in cancer: Expanding the immune effector toolbox. *Immunity* **54**, 2701–2711 (2021).

58. Tamura, T. *et al.* Diverse NKT cells regulate early inflammation and neurological outcomes after cardiac arrest and resuscitation. *Sci. Transl. Med.* **16**, eadq5796 (2024).

59. Zhang, Y. *et al.* Dissecting the heterogeneity and tumor-associated dynamics of human liver group I ILC via scRNA sequencing data. *Immunol. Res.* **73**, 122 (2025).

60. Brauneck, F. *et al.* Immunosuppressive M2 TAMs represent a promising target population to enhance phagocytosis of ovarian cancer cells in vitro. *Front. Immunol.* **14**, 1250258 (2023).

61. Matusiak, M. *et al.* Spatially Segregated Macrophage Populations Predict Distinct Outcomes in Colon Cancer. *Cancer Discov.* **14**, 1418–1439 (2024).

62. Rakina, M., Larionova, I. & Kzhyshkowska, J. Macrophage diversity in human cancers: New insight provided by single-cell resolution and spatial context. *Heliyon* **10**, e28332 (2024).

63. Dong, L. *et al.* SPP1+ TAM Regulates the Metastatic Colonization of CXCR4+ Metastasis-Associated Tumor Cells by Remodeling the Lymph Node Microenvironment. *Adv. Sci.* **11**, 2400524 (2024).

64. Zhang, Q. *et al.* Metabolic and immune crosstalk between cancer-associated fibroblasts and pancreatic cancer cells. *J. Transl. Med.* **23**, 1118 (2025).

65. Yang, S. *et al.* Emerging role of cancer-associated fibroblasts in the premetastatic niche. *Mol. Cancer* **24**, 250 (2025).

66. Piwocka, O., Piotrowski, I., Suchorska, W. M. & Kulcenty, K. Dynamic interactions in the tumor niche: how the cross-talk between CAFs and the tumor microenvironment impacts resistance to therapy. *Front. Mol. Biosci.* **11**, 1343523 (2024).

67. Yang, D., Liu, J., Qian, H. & Zhuang, Q. Cancer-associated fibroblasts: from basic science to anticancer therapy. *Exp. Mol. Med.* **55**, 1322–1332 (2023).

68. Manoukian, P., Bijlsma, M. & van Laarhoven, H. The Cellular Origins of Cancer-Associated Fibroblasts and Their Opposing Contributions to Pancreatic Cancer Growth. *Front. Cell Dev. Biol.* **9**, 743907 (2021).

69. Sahai, E. *et al.* A framework for advancing our understanding of cancer-associated fibroblasts. *Nat. Rev. Cancer* **20**, 174–186 (2020).

70. Kerdidani, D. *et al.* Lung tumor MHCII immunity depends on in situ antigen presentation by fibroblasts. *J. Exp. Med.* **219**, (2022).

71. Hosaka, K. *et al.* Pericyte-fibroblast transition promotes tumor growth and metastasis. *Proc. Natl. Acad. Sci. U. S. A.* **113**, E5618-5627 (2016).

72. Omori, K. *et al.* Inhibition of stromal cell-derived factor-1α/CXCR4 signaling restores the blood-retina barrier in pericyte-deficient mouse retinas. *JCI Insight* **3**, 120706 (2018).

73. Pombero, A., Garcia-Lopez, R. & Martínez, S. Pericyte-Glioblastoma Cell Interaction: A Key Target to Prevent Glioblastoma Progression. *Cells* **12**, (2023).

74. Zhuo, W. *et al.* The CXCL12-CXCR4 chemokine pathway: a novel axis regulates lymphangiogenesis. *Clin. Cancer Res. Off. J. Am. Assoc. Cancer Res.* **18**, 5387–5398 (2012).

75. Wu, F. *et al.* Signaling pathways in cancer-associated fibroblasts and targeted therapy for cancer. *Signal Transduct. Target. Ther.* **6**, 218 (2021).

76. Hua, H., Kong, Q., Yin, J., Zhang, J. & Jiang, Y. Insulin-like growth factor receptor signaling in tumorigenesis and drug resistance: a challenge for cancer therapy. *J. Hematol. Oncol.J Hematol Oncol* **13**, 64 (2020).

77. Chen, Y. *et al.* High p-Smad2 expression in stromal fibroblasts predicts poor survival in patients with clinical stage I to IIIA non-small cell lung cancer. *World J. Surg. Oncol.* **12**, 328 (2014).

78. Stenina-Adognravi, O. & Plow, E. F. Thrombospondin-4 in tissue remodeling. *Matrix Biol. J. Int. Soc. Matrix Biol.* **75–76**, 300–313 (2019).

79. Kim, M. S. *et al.* Potential Role of PDGFRβ-Associated THBS4 in Colorectal Cancer Development. *Cancers* **12**, (2020).

80. Lee, M., Cho, H.-J., Park, K.-S. & Jung, H.-Y. ELK3 Controls Gastric Cancer Cell Migration and Invasion by Regulating ECM Remodeling-Related Genes. *Int. J. Mol. Sci.* **23**, (2022).

81. Peran, I. *et al.* Cadherin 11 Promotes Immunosuppression and Extracellular Matrix Deposition to Support Growth of Pancreatic Tumors and Resistance to Gemcitabine in Mice. *Gastroenterology* **160**, 1359-1372.e13 (2021).

82. Minoura, H., Okamoto, R., Hiki, N. & Yamashita, K. Cancer-Associated Fibroblasts Genes and Transforming Growth Factor Beta Pathway in Gastric Cancer for Novel Therapeutic Strategy. *Cancers* **17**, (2025).

83. Song, J. *et al.* Antigen-presenting cancer associated fibroblasts enhance antitumor immunity and predict immunotherapy response. *Nat. Commun.* **16**, 2175 (2025).

84. Kennel, K. B., Bozlar, M., De Valk, A. F. & Greten, F. R. Cancer-Associated Fibroblasts in Inflammation and Antitumor Immunity. *Clin. Cancer Res. Off. J. Am. Assoc. Cancer Res.* **29**, 1009–1016 (2023).

85. Wang, Y. *et al.* The immune microenvironment in endometrial carcinoma: mechanisms and therapeutic targeting. *Front. Immunol.* **16**, 1586315 (2025).

86. Abdul-Rahman, T. *et al.* The paradoxical role of cytokines and chemokines at the tumor microenvironment: a comprehensive review. *Eur. J. Med. Res.* **29**, 124 (2024).

87. Toledo, B. *et al.* Deciphering the performance of macrophages in tumour microenvironment: a call for precision immunotherapy. *J. Hematol. Oncol.J Hematol Oncol* **17**, 44 (2024).

88. Deshmane, S. L., Kremlev, S., Amini, S. & Sawaya, B. E. Monocyte chemoattractant protein-1 (MCP-1): an overview. *J. Interferon Cytokine Res. Off. J. Int. Soc. Interferon Cytokine Res.* **29**, 313–326 (2009).

89. Cui, H., Hamad, M. & Elkord, E. TIGIT in cancer: from mechanism of action to promising immunotherapeutic strategies. *Cell Death Dis.* **16**, 664 (2025).

90. Qian, D. *et al.* Immunotherapeutic strategies targeting the PVR-TIGIT/CD96/CD226 signaling pathway in glioma treatment. *Ann. Med.* **57**, 2588717 (2025).

91. Garg, V. *et al.* Elucidating divergent biology in uterine carcinosarcoma. *Transl. Oncol.* **61**, 102506 (2025).

92. da Silva, J. L. *et al.* The prevalence and prognostic impact of tumor-infiltrating lymphocytes in uterine carcinosarcoma. *BMC Cancer* **21**, 1306 (2021).

93. Shaker, N., Chen, W., Sinclair, W., Parwani, A. V. & Li, Z. Identifying SOX17 as a Sensitive and Specific Marker for Ovarian and Endometrial Carcinomas. *Mod. Pathol. Off. J. U. S. Can. Acad. Pathol. Inc* **36**, 100038 (2023).

94. De Tommasi, O. *et al.* PD-1 and PD-L1 Expression in Endometrial Cancer: A Systematic Review of the Literature. *J. Clin. Med.* **14**, 401 (2025).

95. Santoro, A. *et al.* The emerging and challenging role of PD-L1 in patients with gynecological cancers: An updating review with clinico-pathological considerations. *Gynecol. Oncol.* **184**, 57–66 (2024).

96. Kaya, M., Schaddelee, M. C. A., Creutzberg, C. L., Kroep, J. R. & Horeweg, N. Efficacy of PD-(L)1 inhibition in the treatment of endometrial cancer across molecular classes: a systematic review and meta-analysis. *Int. J. Gynecol. Cancer* **35**, 101759 (2025).

97. Sulaiman, R. *et al.* Characterization and Clinical Relevance of Endometrial CAFs: Correlation between Post-Surgery Event and Resistance to Drugs. *Int. J. Mol. Sci.* **24**, (2023).

98. McKenna, A. *et al.* The Genome Analysis Toolkit: a MapReduce framework for analyzing next-generation DNA sequencing data. *Genome Res.* **20**, 1297–1303 (2010).

99. Zhang, L. & Zhang, L. Use of autocorrelation scanning in DNA copy number analysis. *Bioinforma. Oxf. Engl.* **29**, 2678–2682 (2013).

100. Bergmann, E. A., Chen, B.-J., Arora, K., Vacic, V. & Zody, M. C. Conpair: concordance and contamination estimator for matched tumor-normal pairs. *Bioinforma. Oxf. Engl.* **32**, 3196–3198 (2016).

101. Cibulskis, K. *et al.* Sensitive detection of somatic point mutations in impure and heterogeneous cancer samples. *Nat. Biotechnol.* **31**, 213–219 (2013).

102. Kim, S. *et al.* Strelka2: fast and accurate calling of germline and somatic variants. *Nat. Methods* **15**, 591–594 (2018).

103. Narzisi, G. *et al.* Genome-wide somatic variant calling using localized colored de Bruijn graphs. *Commun. Biol.* **1**, 20 (2018).

104. Wala, J. A. *et al.* SvABA: genome-wide detection of structural variants and indels by local assembly. *Genome Res.* **28**, 581–591 (2018).

105. Chen, X. *et al.* Manta: rapid detection of structural variants and indels for germline and cancer sequencing applications. *Bioinforma. Oxf. Engl.* **32**, 1220–1222 (2016).

106. Layer, R. M., Chiang, C., Quinlan, A. R. & Hall, I. M. LUMPY: a probabilistic framework for structural variant discovery. *Genome Biol.* **15**, R84 (2014).

107. Xi, R., Lee, S., Xia, Y., Kim, T.-M. & Park, P. J. Copy number analysis of whole-genome data using BIC-seq2 and its application to detection of cancer susceptibility variants. *Nucleic Acids Res.* **44**, 6274–6286 (2016).

108. Quinlan, A. R. & Hall, I. M. BEDTools: a flexible suite of utilities for comparing genomic features. *Bioinforma. Oxf. Engl.* **26**, 841–842 (2010).

109. Tate, J. G. *et al.* COSMIC: the Catalogue Of Somatic Mutations In Cancer. *Nucleic Acids Res.* **47**, D941–D947 (2019).

110. Auton, A. *et al.* A global reference for human genetic variation. *Nature* **526**, 68–74 (2015).

111. Landrum, M. J. *et al.* ClinVar: public archive of relationships among sequence variation and human phenotype. *Nucleic Acids Res.* **42**, D980-985 (2014).

112. Adzhubei, I., Jordan, D. M. & Sunyaev, S. R. Predicting functional effect of human missense mutations using PolyPhen-2. *Curr. Protoc. Hum. Genet.* **Chapter 7**, Unit7.20 (2013).

113. Vaser, R., Adusumalli, S., Leng, S. N., Sikic, M. & Ng, P. C. SIFT missense predictions for genomes. *Nat. Protoc.* **11**, 1–9 (2016).

114. Shihab, H. A. *et al.* Ranking non-synonymous single nucleotide polymorphisms based on disease concepts. *Hum. Genomics* **8**, 11 (2014).

115. Lek, M. *et al.* Analysis of protein-coding genetic variation in 60,706 humans. *Nature* **536**, 285–291 (2016).

116. Sherry, S. T. *et al.* dbSNP: the NCBI database of genetic variation. *Nucleic Acids Res.* **29**, 308–311 (2001).

117. McLaren, W. *et al.* The Ensembl Variant Effect Predictor. *Genome Biol.* **17**, 122 (2016).

118. Hubbard, T. *et al.* The Ensembl genome database project. *Nucleic Acids Res.* **30**, 38–41 (2002).

119. Jeffares, D. C. *et al.* Transient structural variations have strong effects on quantitative traits and reproductive isolation in fission yeast. *Nat. Commun.* **8**, 14061 (2017).

120. Sondka, Z. *et al.* COSMIC: a curated database of somatic variants and clinical data for cancer. *Nucleic Acids Res.* **52**, D1210–D1217 (2024).

121. Katcher, A. *et al.* Establishing patient-derived organoids from human endometrial cancer and normal endometrium. *Front. Endocrinol.* **14**, 1059228 (2023).

122. Barbi, M. *et al.* Generation and Maintenance of Patient-Derived Endometrial Cancer Organoids. *Bio-Protoc.* **14**, e5093 (2024).

123. Xu, J. *et al.* Single-Cell RNA Sequencing Reveals the Tissue Architecture in Human High-Grade Serous Ovarian Cancer. *Clin. Cancer Res. Off. J. Am. Assoc. Cancer Res.* **28**, 3590–3602 (2022).

124. Gao, R. *et al.* Delineating copy number and clonal substructure in human tumors from single-cell transcriptomes. *Nat. Biotechnol.* **39**, 599–608 (2021).

125. Jin, S. *et al.* Inference and analysis of cell-cell communication using CellChat. *Nat. Commun.* **12**, 1088 (2021).

126. Squair, J. W. *et al.* Confronting false discoveries in single-cell differential expression. *Nat. Commun.* **12**, 5692 (2021).

127. Subhash, S. & Kanduri, C. GeneSCF: a real-time based functional enrichment tool with support for multiple organisms. *BMC Bioinformatics* **17**, 365 (2016).

128. Bailey, T. L., Johnson, J., Grant, C. E. & Noble, W. S. The MEME Suite. *Nucleic Acids Res.* **43**, W39-49 (2015).

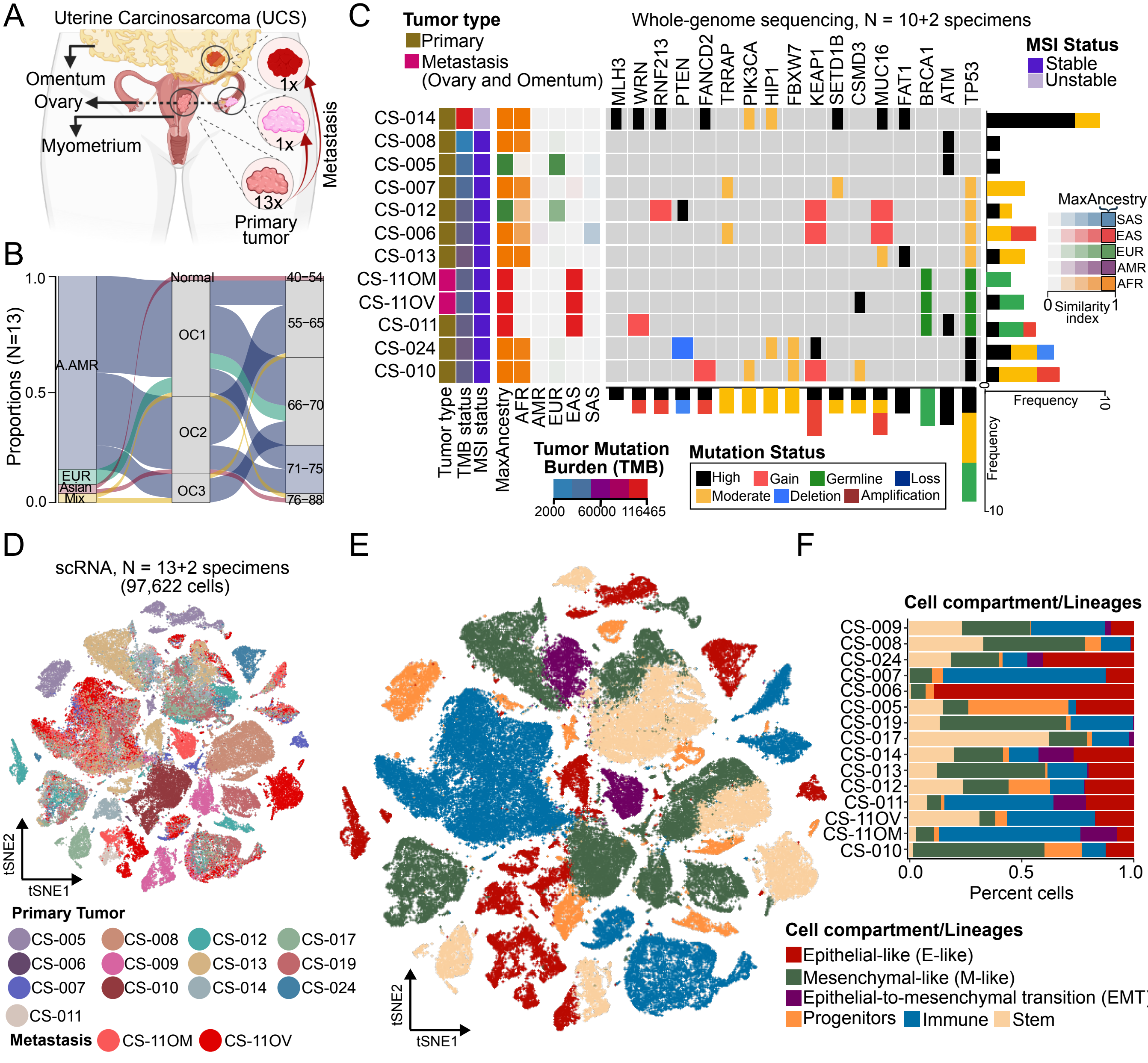
A
Uterine Carcinosarcoma (UCS)
Omentum
Ovary
Myometrium
1x
1x
13x
Primary tumor
Metastasis
B
Proportions (N=13)
1.0
0.5
0.0
A.AMR
EUR
Asian
Mix
Normal
OC1
OC2
OC3
40–54
55–65
66–70
71–75
76–88
C
Tumor type
Primary
Metastasis (Ovary and Omentum)
Whole-genome sequencing, N = 10+2 specimens
MSI Status
Stable
Unstable
MLH3
WRN
RNF213
PTEN
FANCD2
TRRAP
PIK3CA
HIP1
FBXW7
KEAP1
SETD1B
CSMD3
MUC16
FAT1
BRCA1
ATM
TP53
CS-014
CS-008
CS-005
CS-007
CS-012
CS-006
CS-013
CS-11OM
CS-11OV
CS-011
CS-024
CS-010
Tumor type
TMB status
MSI status
MaxAncestry
AFR
AMR
EUR
EAS
SAS
MaxAncestry
SAS
EAS
EUR
AMR
AFR
0
Similarity index
1
0
Frequency
10
Frequency
10
Tumor Mutation Burden (TMB)
2000
60000
116465
Mutation Status
High
Gain
Germline
Loss
Moderate
Deletion
Amplification
D
scRNA, N = 13+2 specimens (97,622 cells)
tSNE2
tSNE1
Primary Tumor
CS-005
CS-008
CS-012
CS-017
CS-006
CS-009
CS-013
CS-019
CS-007
CS-010
CS-014
CS-024
CS-011
Metastasis
CS-11OM
CS-11OV
E
tSNE2
tSNE1
F
Cell compartment/Lineages
CS-009
CS-008
CS-024
CS-007
CS-006
CS-005
CS-019
CS-017
CS-014
CS-013
CS-012
CS-011
CS-11OV
CS-11OM
CS-010
0.0
0.5
1.0
Percent cells
Cell compartment/Lineages
Epithelial-like (E-like)
Mesenchymal-like (M-like)
Epithelial-to-mesenchymal transition (EMT)
Progenitors
Immune
Stem

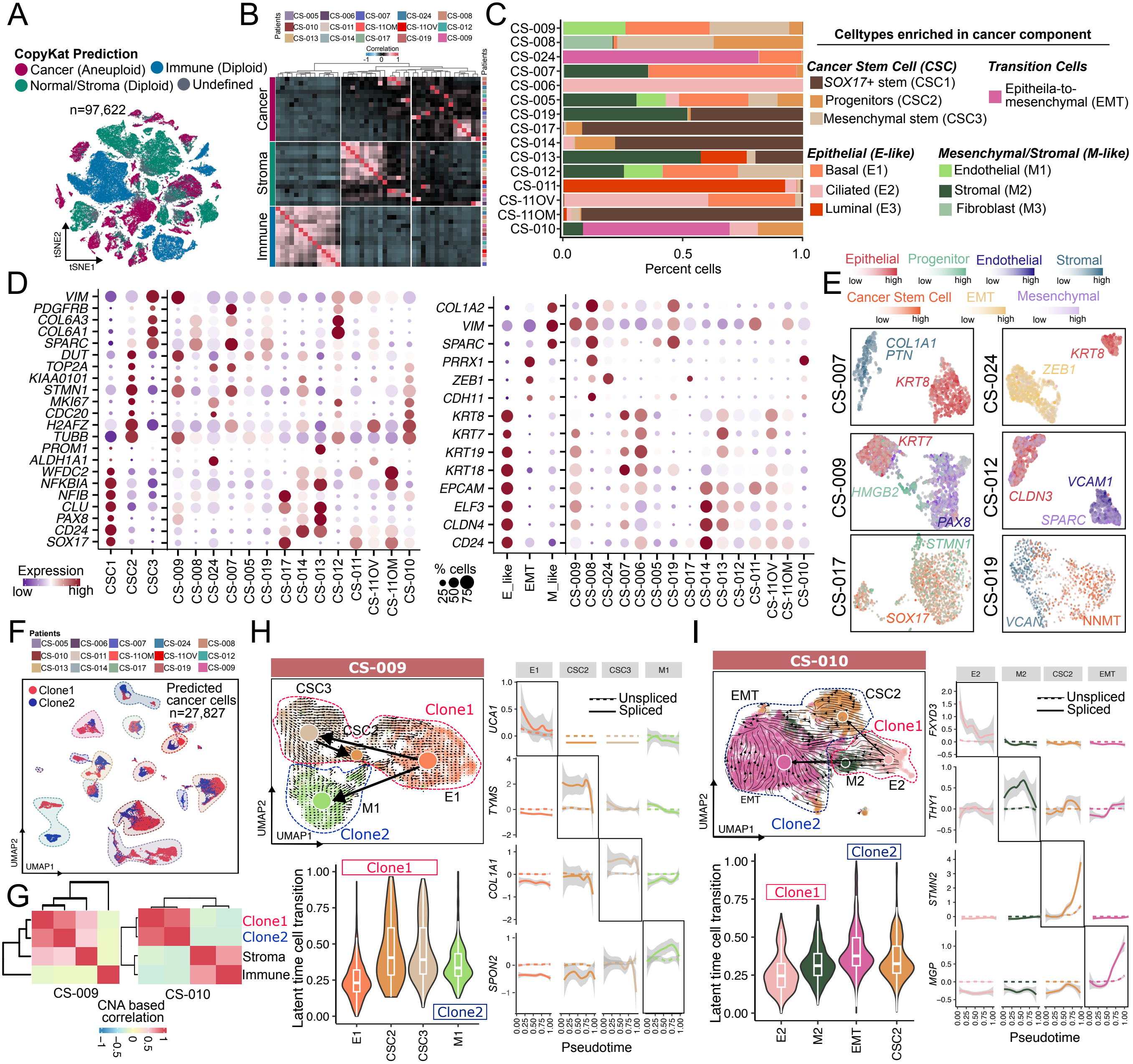
A
CopyKat Prediction
Cancer (Aneuploid)
Immune (Diploid)
Normal/Stroma (Diploid)
Undefined
n=97,622
tSNE2
tSNE1
B
Patients
CS-005 CS-006 CS-007 CS-024 CS-008
CS-010 CS-011 CS-11OM CS-11OV CS-012
CS-013 CS-014 CS-017 CS-019 CS-009
Correlation
-1 0 1
Cancer
Stroma
Immune
C
CS-009 CS-008 CS-024 CS-007 CS-006 CS-005 CS-019 CS-017 CS-014 CS-013 CS-012 CS-011 CS-11OV CS-11OM CS-010
0.0 0.5 1.0
Percent cells
Celltypes enriched in cancer component
Cancer Stem Cell (CSC)
SOX17+ stem (CSC1)
Progenitors (CSC2)
Mesenchymal stem (CSC3)
Transition Cells
Epitheila-to-mesenchymal (EMT)
Epithelial (E-like)
Basal (E1)
Ciliated (E2)
Luminal (E3)
Mesenchymal/Stromal (M-like)
Endothelial (M1)
Stromal (M2)
Fibroblast (M3)
D
VIM PDGFRB COL6A3 COL6A1 SPARC DUT TOP2A KIAA0101 STMN1 MKI67 CDC20 H2AFZ TUBB PROM1 ALDH1A1 WFDC2 NFKBIA NFIB CLU PAX8 CD24 SOX17
CSC1 CSC2 CSC3 CS-009 CS-008 CS-024 CS-007 CS-005 CS-019 CS-017 CS-014 CS-013 CS-012 CS-011 CS-11OV CS-11OM CS-010
Expression
low high
% cells
25 50 75
COL1A2 VIM SPARC PRRX1 ZEB1 CDH11 KRT8 KRT7 KRT19 KRT18 EPCAM ELF3 CLDN4 CD24
E_like EMT M_like CS-009 CS-008 CS-024 CS-007 CS-006 CS-005 CS-019 CS-017 CS-014 CS-013 CS-012 CS-011 CS-11OV CS-11OM CS-010
E
Epithelial low high
Progenitor low high
Endothelial low high
Stromal low high
Cancer Stem Cell low high
EMT low high
Mesenchymal low high
CS-007 COL1A1 PTN KRT8
CS-024 KRT8 ZEB1
CS-009 KRT7 HMGB2 PAX8
CS-012 CLDN3 VCAM1 SPARC
CS-017 STMN1 SOX17
CS-019 VCAN NNMT
F
Patients
CS-005 CS-006 CS-007 CS-024 CS-008
CS-010 CS-011 CS-11OM CS-11OV CS-012
CS-013 CS-014 CS-017 CS-019 CS-009
Clone1
Clone2
Predicted cancer cells n=27,827
UMAP2
UMAP1
G
Clone1
Clone2
Stroma
Immune
CS-009
CS-010
CNA based correlation
-1 -0.5 0 0.5 1
H
CS-009
CSC3
CSC2
Clone1
E1
M1
Clone2
UMAP2
UMAP1
Latent time cell transition
0.00 0.25 0.50 0.75 1.00
Clone1
Clone2
E1 CSC2 CSC3 M1
E1 CSC2 CSC3 M1
Unspliced
Spliced
UCA1
TYMS
COL1A1
SPON2
Pseudotime
0.00 0.25 0.50 0.75 1.00
I
CS-010
EMT
CSC2
Clone1
M2
E2
Clone2
UMAP2
UMAP1
Latent time cell transition
0.00 0.25 0.50 0.75 1.00
Clone1
Clone2
E2 M2 EMT CSC2
E2 M2 CSC2 EMT
Unspliced
Spliced
FXYD3
THY1
STMN2
MGP
Pseudotime
0.00 0.25 0.50 0.75 1.00

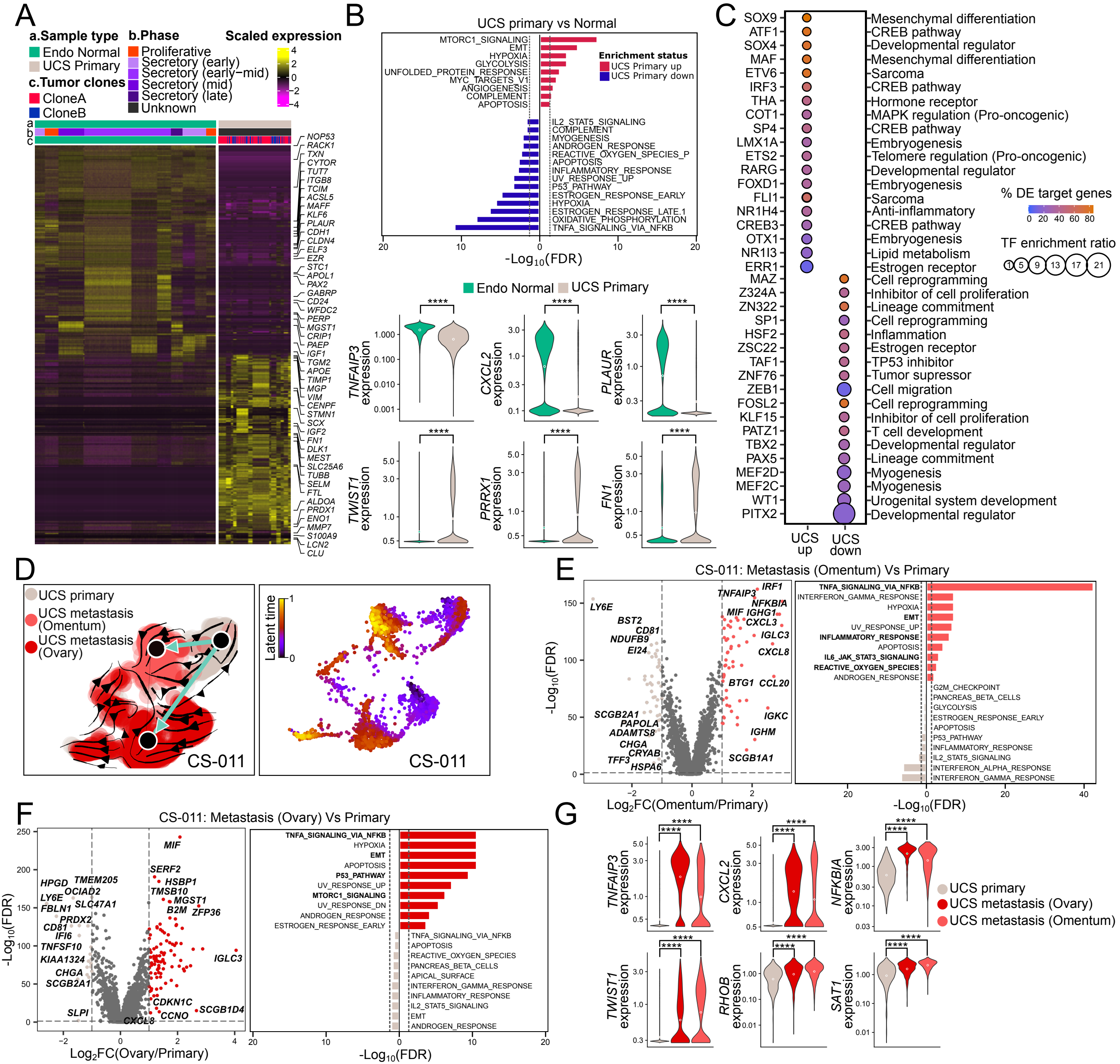
A
a.Sample type
Endo Normal
UCS Primary
b.Phase
Proliferative
Secretory (early)
Secretory (early−mid)
Secretory (mid)
Secretory (late)
Unknown
c.Tumor clones
CloneA
CloneB
Scaled expression
4
2
0
−2
−4
a
b
c
NOP53
RACK1
TXN
CYTOR
TUT7
ITGB8
TCIM
ACSL5
MAFF
KLF6
PLAUR
CDH1
CLDN4
ELF3
EZR
STC1
APOL1
PAX2
GABRP
CD24
WFDC2
PERP
MGST1
CRIP1
PAEP
IGF1
TGM2
APOE
TIMP1
MGP
VIM
CENPF
STMN1
SCX
IGF2
FN1
DLK1
MEST
SLC25A6
TUBB
SELM
FTL
ALDOA
PRDX1
ENO1
MMP7
S100A9
LCN2
CLU
B
UCS primary vs Normal
MTORC1_SIGNALING
EMT
HYPOXIA
GLYCOLYSIS
UNFOLDED_PROTEIN_RESPONSE
MYC_TARGETS_V1
ANGIOGENESIS
COMPLEMENT
APOPTOSIS
IL2_STAT5_SIGNALING
COMPLEMENT
MYOGENESIS
ANDROGEN_RESPONSE
REACTIVE_OXYGEN_SPECIES_P
APOPTOSIS
INFLAMMATORY_RESPONSE
UV_RESPONSE_UP
P53_PATHWAY
ESTROGEN_RESPONSE_EARLY
HYPOXIA
ESTROGEN_RESPONSE_LATE.1
OXIDATIVE_PHOSPHORYLATION
TNFA_SIGNALING_VIA_NFKB
Enrichment status
UCS Primary up
UCS Primary down
20
10
0
10
20
-Log10(FDR)
Endo Normal
UCS Primary
****
TNFAIP3 expression
1.000
0.100
0.010
0.001
CXCL2 expression
3.0
1.0
0.3
0.1
PLAUR expression
3.0
1.0
0.3
TWIST1 expression
5.0
3.0
1.0
0.5
PRRX1 expression
5.0
3.0
1.0
0.5
FN1 expression
5.0
3.0
1.0
0.5
C
SOX9
ATF1
SOX4
MAF
ETV6
IRF3
THA
COT1
SP4
LMX1A
ETS2
RARG
FOXD1
FLI1
NR1H4
CREB3
OTX1
NR1I3
ERR1
MAZ
Z324A
ZN322
SP1
HSF2
ZSC22
TAF1
ZNF76
ZEB1
FOSL2
KLF15
PATZ1
TBX2
PAX5
MEF2D
MEF2C
WT1
PITX2
UCS up
UCS down
Mesenchymal differentiation
CREB pathway
Developmental regulator
Mesenchymal differentiation
Sarcoma
CREB pathway
Hormone receptor
MAPK regulation (Pro-oncogenic)
CREB pathway
Embryogenesis
Telomere regulation (Pro-oncogenic)
Developmental regulator
Embryogenesis
Sarcoma
Anti-inflammatory
CREB pathway
Embryogenesis
Lipid metabolism
Estrogen receptor
Cell reprogramming
Inhibitor of cell proliferation
Lineage commitment
Cell reprogramming
Inflammation
Estrogen receptor
TP53 inhibitor
Tumor suppressor
Cell migration
Cell reprogramming
Inhibitor of cell proliferation
T cell development
Developmental regulator
Lineage commitment
Myogenesis
Myogenesis
Urogenital system development
Developmental regulator
% DE target genes
0 20 40 60 80
TF enrichment ratio
1 5 9 13 17 21
D
UCS primary
UCS metastasis (Omentum)
UCS metastasis (Ovary)
CS-011
Latent time
1
0
CS-011
E
CS-011: Metastasis (Omentum) Vs Primary
150
100
50
0
-Log10(FDR)
LY6E
BST2
CD81
NDUFB9
EI24
SCGB2A1
PAPOLA
ADAMTS8
CHGA
CRYAB
TFF3
HSPA6
TNFAIP3
IRF1
NFKBIA
MIF
IGHG1
CXCL3
IGLC3
CXCL8
BTG1
CCL20
IGKC
IGHM
SCGB1A1
−2
0
2
Log2FC(Omentum/Primary)
TNFA_SIGNALING_VIA_NFKB
INTERFERON_GAMMA_RESPONSE
HYPOXIA
EMT
UV_RESPONSE_UP
INFLAMMATORY_RESPONSE
APOPTOSIS
IL6_JAK_STAT3_SIGNALING
REACTIVE_OXYGEN_SPECIES
ANDROGEN_RESPONSE
G2M_CHECKPOINT
PANCREAS_BETA_CELLS
GLYCOLYSIS
ESTROGEN_RESPONSE_EARLY
APOPTOSIS
P53_PATHWAY
INFLAMMATORY_RESPONSE
IL2_STAT5_SIGNALING
INTERFERON_ALPHA_RESPONSE
INTERFERON_GAMMA_RESPONSE
20
0
20
40
-Log10(FDR)
F
CS-011: Metastasis (Ovary) Vs Primary
250
200
150
100
50
0
-Log10(FDR)
HPGD
TMEM205
OCIAD2
LY6E
SLC47A1
FBLN1
PRDX2
CD81
IFI6
TNFSF10
KIAA1324
CHGA
SCGB2A1
SLPI
MIF
SERF2
HSBP1
TMSB10
MGST1
B2M
ZFP36
IGLC3
CDKN1C
CCNO
SCGB1D4
CXCL8
−2
0
2
4
Log2FC(Ovary/Primary)
TNFA_SIGNALING_VIA_NFKB
HYPOXIA
EMT
APOPTOSIS
P53_PATHWAY
UV_RESPONSE_UP
MTORC1_SIGNALING
UV_RESPONSE_DN
ANDROGEN_RESPONSE
ESTROGEN_RESPONSE_EARLY
TNFA_SIGNALING_VIA_NFKB
APOPTOSIS
REACTIVE_OXYGEN_SPECIES
PANCREAS_BETA_CELLS
APICAL_SURFACE
INTERFERON_GAMMA_RESPONSE
INFLAMMATORY_RESPONSE
IL2_STAT5_SIGNALING
EMT
ANDROGEN_RESPONSE
20
10
0
10
20
-Log10(FDR)
G
****
TNFAIP3 expression
5.0
3.0
1.0
0.5
CXCL2 expression
5.0
3.0
1.0
0.5
NFKBIA expression
3.00
1.00
0.30
0.10
0.03
TWIST1 expression
3.0
1.0
0.3
RHOB expression
1.00
0.10
0.01
SAT1 expression
1.00
0.10
0.01
UCS primary
UCS metastasis (Ovary)
UCS metastasis (Omentum)

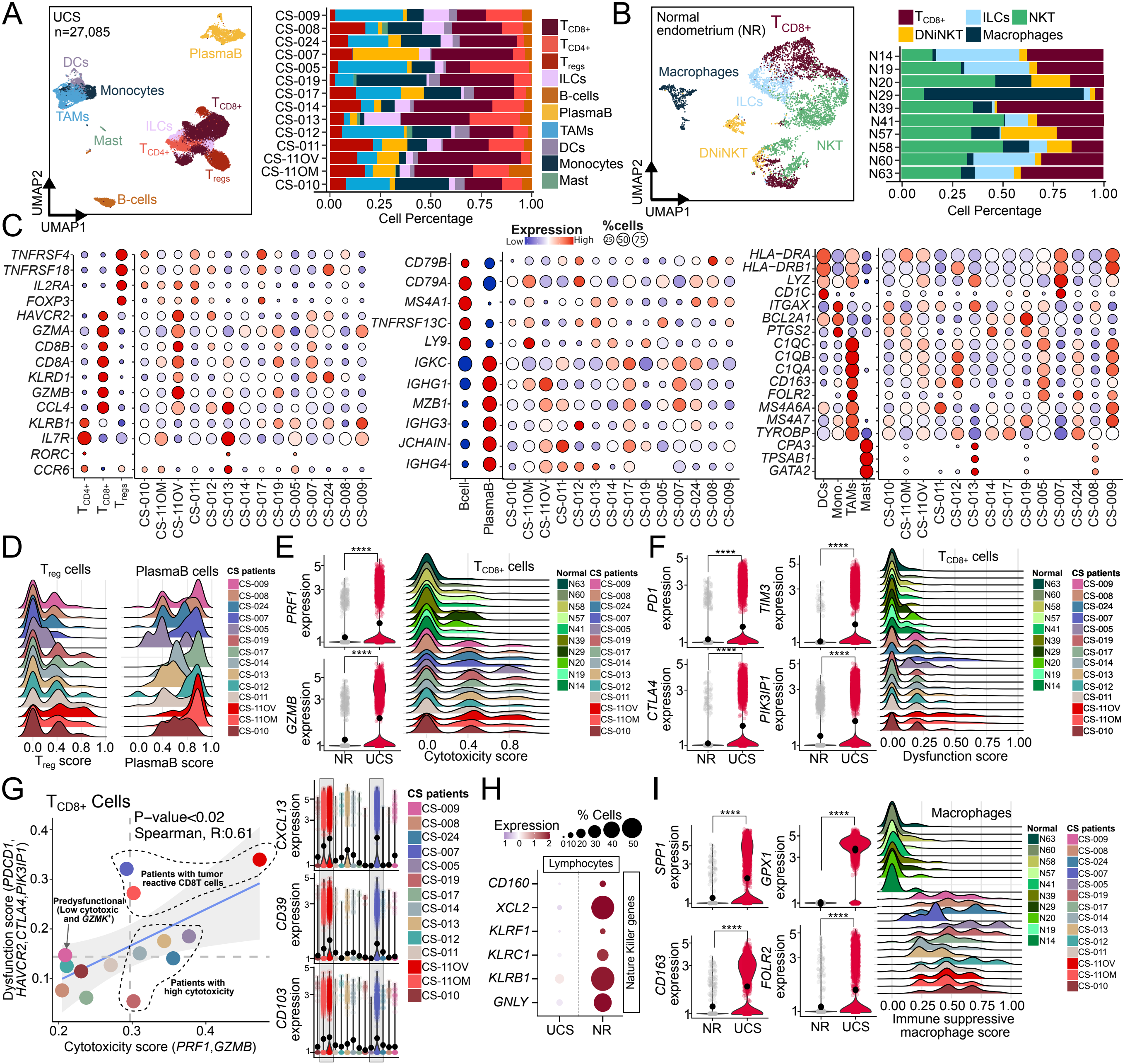
A
UCS
n=27,085
PlasmaB
DCs
Monocytes
TAMs
Mast
ILCs
T_{CD8+}
T_{CD4+}
T_{regs}
B-cells
UMAP1
UMAP2
CS-009
CS-008
CS-024
CS-007
CS-005
CS-019
CS-017
CS-014
CS-013
CS-012
CS-011
CS-11OV
CS-11OM
CS-010
0.00
0.25
0.50
0.75
1.00
Cell Percentage
T_{CD8+}
T_{CD4+}
T_{regs}
ILCs
B-cells
PlasmaB
TAMs
DCs
Monocytes
Mast
B
Normal endometrium (NR)
T_{CD8+}
Macrophages
ILCs
DNiNKT
NKT
UMAP1
UMAP2
T_{CD8+}
ILCs
NKT
DNiNKT
Macrophages
N14
N19
N20
N29
N39
N41
N57
N58
N60
N63
0.00
0.25
0.50
0.75
1.00
Cell Percentage
C
Expression
Low
High
%cells
25
50
75
TNFRSF4
TNFRSF18
IL2RA
FOXP3
HAVCR2
GZMA
CD8B
CD8A
KLRD1
GZMB
CCL4
KLRB1
IL7R
RORC
CCR6
T_{CD4+}
T_{CD8+}
T_{regs}
CD79B
CD79A
MS4A1
TNFRSF13C
LY9
IGKC
IGHG1
MZB1
IGHG3
JCHAIN
IGHG4
Bcell
PlasmaB
HLA−DRA
HLA−DRB1
LYZ
CD1C
ITGAX
BCL2A1
PTGS2
C1QC
C1QB
C1QA
CD163
FOLR2
MS4A6A
MS4A7
TYROBP
CPA3
TPSAB1
GATA2
DCs
Mono.
TAMs
Mast
CS-010
CS-11OM
CS-11OV
CS-011
CS-012
CS-013
CS-014
CS-017
CS-019
CS-005
CS-007
CS-024
CS-008
CS-009
D
T_{reg} cells
PlasmaB cells
CS patients
0.0
0.4
0.8
1.0
T_{reg} score
PlasmaB score
E
PRF1 expression
GZMB expression
****
NR
UCS
T_{CD8+} cells
Cytotoxicity score
Normal
CS patients
N63
N60
N58
N57
N41
N39
N29
N20
N19
N14
F
PD1 expression
TIM3 expression
CTLA4 expression
PIK3IP1 expression
****
NR
UCS
T_{CD8+} cells
Dysfunction score
G
T_{CD8+} Cells
P−value<0.02
Spearman, R:0.61
Patients with tumor reactive CD8T cells
Predysfunctional (Low cytotoxic and GZMK⁺)
Patients with high cytotoxicity
Dysfunction score (PDCD1, HAVCR2, CTLA4, PIK3IP1)
Cytotoxicity score (PRF1, GZMB)
0.1
0.2
0.3
0.4
CXCL13 expression
CD39 expression
CD103 expression
CS patients
H
Expression
% Cells
Lymphocytes
CD160
XCL2
KLRF1
KLRC1
KLRB1
GNLY
Nature Killer genes
UCS
NR
I
SPP1 expression
GPX1 expression
CD163 expression
FOLR2 expression
****
NR
UCS
Macrophages
Immune suppressive macrophage score
Normal
CS patients

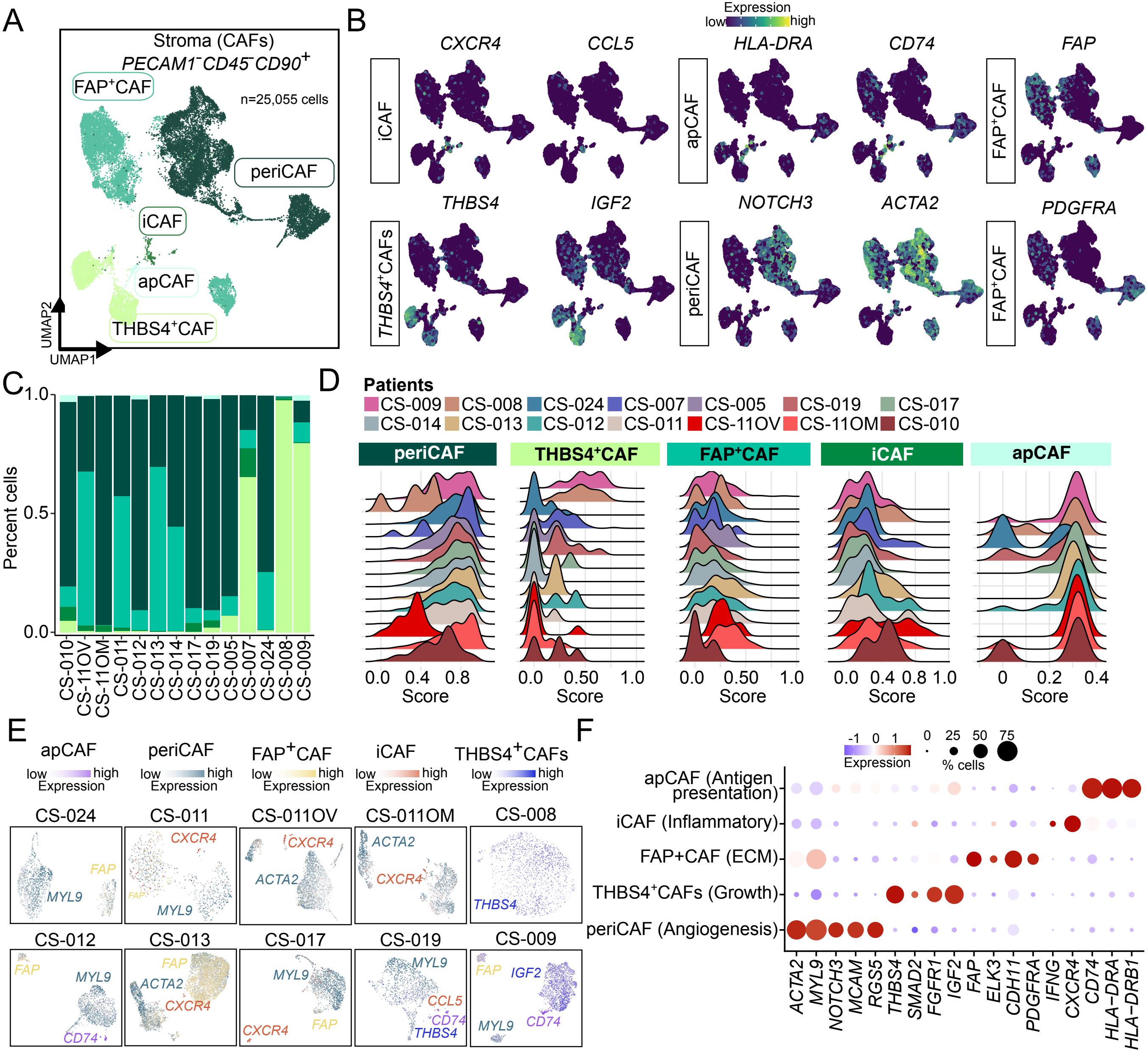
A
Stroma (CAFs)
PECAM1⁻CD45⁻CD90⁺
FAP⁺CAF
n=25,055 cells
periCAF
iCAF
apCAF
THBS4⁺CAF
UMAP2
UMAP1
B
Expression
low
high
CXCR4
CCL5
HLA-DRA
CD74
FAP
THBS4
IGF2
NOTCH3
ACTA2
PDGFRA
iCAF
apCAF
FAP⁺CAF
THBS4⁺CAFs
periCAF
C
Percent cells
1.0
0.5
0.0
CS-010
CS-11OV
CS-11OM
CS-011
CS-012
CS-013
CS-014
CS-017
CS-019
CS-005
CS-007
CS-024
CS-008
CS-009
D
Patients
CS-009
CS-008
CS-024
CS-007
CS-005
CS-019
CS-017
CS-014
CS-013
CS-012
CS-011
CS-11OV
CS-11OM
CS-010
periCAF
THBS4⁺CAF
FAP⁺CAF
iCAF
apCAF
0.0
0.4
0.8
0.50
1.0
0
0.2
Score
E
apCAF
periCAF
FAP⁺CAF
iCAF
THBS4⁺CAFs
low
high
Expression
CS-024
CS-011
CS-011OV
CS-011OM
CS-008
CS-012
CS-013
CS-017
CS-019
CS-009
FAP
MYL9
CXCR4
ACTA2
THBS4
CD74
CCL5
IGF2
F
-1
0
1
Expression
0
25
50
75
% cells
apCAF (Antigen presentation)
iCAF (Inflammatory)
FAP+CAF (ECM)
THBS4⁺CAFs (Growth)
periCAF (Angiogenesis)
ACTA2
MYL9
NOTCH3
MCAM
RGS5
THBS4
SMAD2
FGFR1
IGF2
FAP
ELK3
CDH11
PDGFRA
IFNG
CXCR4
CD74
HLA-DRA
HLA-DRB1

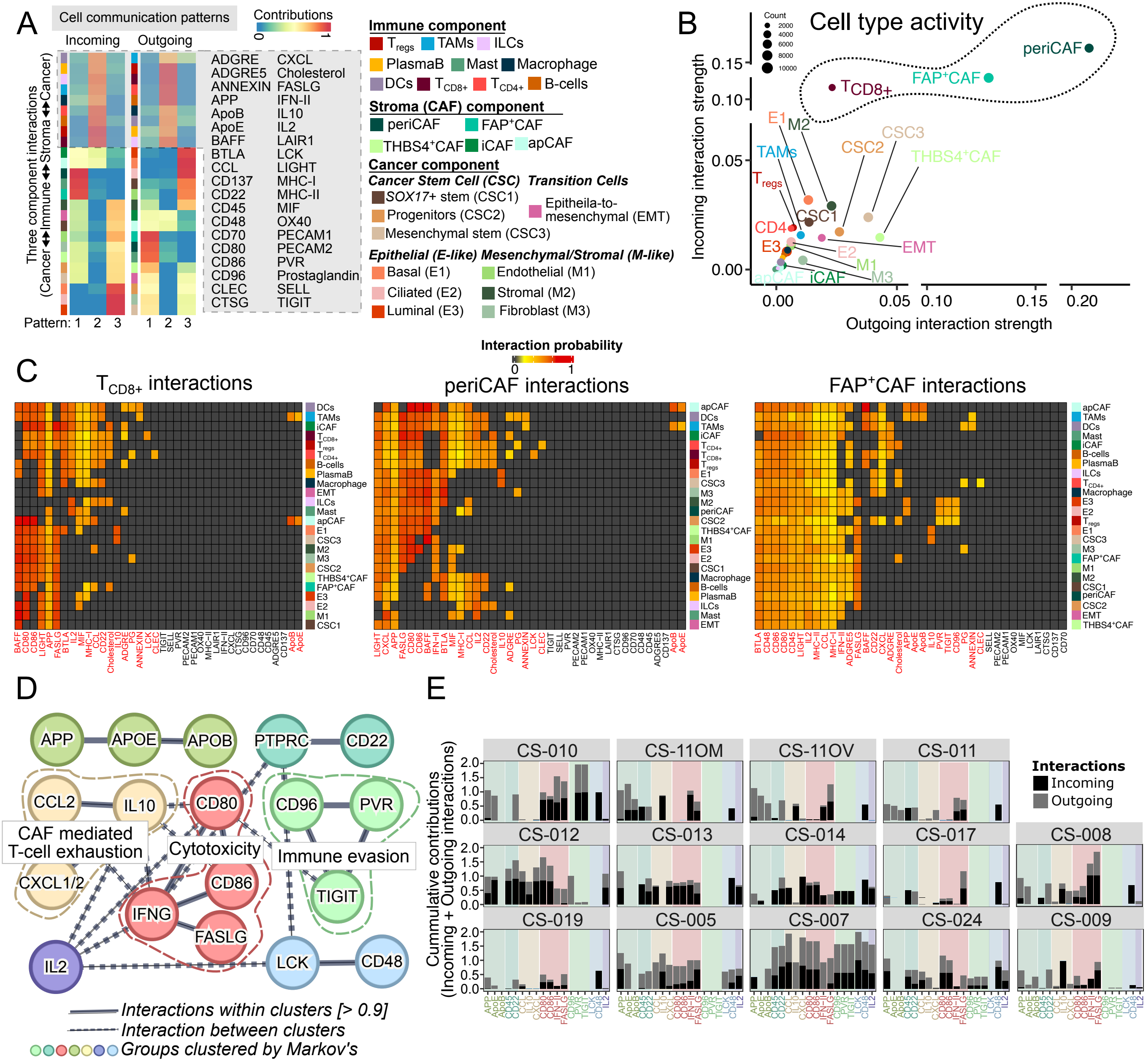
A
Cell communication patterns
Contributions
0
1
Incoming
Outgoing
Three component interactions
(Cancer ⟷ Immune ⟷ Stroma ⟷ Cancer)
Pattern: 1 2 3
1 2 3
ADGRE
ADGRE5
ANNEXIN
APP
ApoB
ApoE
BAFF
BTLA
CCL
CD137
CD22
CD45
CD48
CD70
CD80
CD86
CD96
CLEC
CTSG
CXCL
Cholesterol
FASLG
IFN-II
IL10
IL2
LAIR1
LCK
LIGHT
MHC-I
MHC-II
MIF
OX40
PECAM1
PECAM2
PVR
Prostaglandin
SELL
TIGIT
Immune component
Tregs
TAMs
ILCs
PlasmaB
Mast
Macrophage
DCs
TCD8+
TCD4+
B-cells
Stroma (CAF) component
periCAF
FAP+CAF
THBS4+CAF
iCAF
apCAF
Cancer component
Cancer Stem Cell (CSC)
Transition Cells
SOX17+ stem (CSC1)
Progenitors (CSC2)
Mesenchymal stem (CSC3)
Epitheila-to-mesenchymal (EMT)
Epithelial (E-like)
Mesenchymal/Stromal (M-like)
Basal (E1)
Ciliated (E2)
Luminal (E3)
Endothelial (M1)
Stromal (M2)
Fibroblast (M3)
B
Cell type activity
Count
2000
4000
6000
8000
10000
periCAF
FAP+CAF
TCD8+
E1
M2
CSC3
CSC2
THBS4+CAF
TAMs
Tregs
CSC1
CD4
E3
E2
EMT
M1
M3
apCAF
iCAF
Incoming interaction strength
0.00
0.05
0.10
0.15
Outgoing interaction strength
0.00
0.05
0.10
0.15
0.20
C
Interaction probability
0
1
TCD8+ interactions
periCAF interactions
FAP+CAF interactions
DCs
TAMs
iCAF
TCD8+
Tregs
TCD4+
B-cells
PlasmaB
Macrophage
EMT
M3
ILCs
Mast
apCAF
E1
CSC3
M2
M3
CSC2
THBS4+CAF
FAP+CAF
E3
E2
M1
CSC1
BAFF
CD80
CD86
LIGHT
APP
FASLG
IL2
BTLA
MIF
MHC-I
CCL
CD22
Cholesterol
IL10
ADGRE
PG
ANNEXIN
LCK
CLEC
TIGIT
SELL
PVR
PECAM2
PECAM1
OX40
MHC-II
LAIR1
CXCL
CTSG
CD96
CD70
CD48
CD45
ADGRE5
CD137
ApoB
ApoE
apCAF
DCs
TAMs
iCAF
TCD4+
TCD8+
Tregs
E1
CSC3
M3
M2
periCAF
CSC2
THBS4+CAF
M1
E3
E2
CSC1
Macrophage
B-cells
PlasmaB
ILCs
Mast
EMT
LIGHT
CXCL
APP
FASLG
CD80
CD86
BAFF
IFN-II
BTLA
MIF
MHC-I
CCL
IL2
CD22
Cholesterol
IL10
ADGRE
PG
ANNEXIN
LCK
CLEC
TIGIT
SELL
PVR
PECAM2
OX40
MHC-II
LAIR1
CTSG
CD96
CD70
CD48
CD45
ADGRE5
CD137
ApoB
ApoE
apCAF
TAMs
DCs
Mast
iCAF
B-cells
PlasmaB
ILCs
TCD4+
Macrophage
E3
E2
Tregs
E1
CSC3
M3
FAP+CAF
M1
M2
CSC1
periCAF
CSC2
EMT
THBS4+CAF
BTLA
CD48
CD80
CD86
CD45
LIGHT
IL2
MHC-II
CD22
MHC-I
IFN-II
ADGRE5
FASLG
BAFF
CCL
CXCL
ADGRE
Cholesterol
APP
ApoE
ApoB
IL10
PVR
TIGIT
CD96
PG
ANNEXIN
CLEC
SELL
PECAM2
PECAM1
OX40
MIF
LCK
LAIR1
CTSG
CD137
CD70
D
APP
APOE
APOB
PTPRC
CD22
CCL2
IL10
CD80
CD96
PVR
CAF mediated
T-cell exhaustion
Cytotoxicity
Immune evasion
CXCL1/2
CD86
TIGIT
IFNG
FASLG
IL2
LCK
CD48
Interactions within clusters [> 0.9]
Interaction between clusters
Groups clustered by Markov's
E
Cummulative contributions
(Incoming + Outgoing interacitions)
CS-010
CS-11OM
CS-11OV
CS-011
CS-012
CS-013
CS-014
CS-017
CS-008
CS-019
CS-005
CS-007
CS-024
CS-009
0.0
0.5
1.0
1.5
2.0
Interactions
Incoming
Outgoing
APP
ApoE
ApoB
CD45
CD22
CCL
IL10
CXCL
CD80
CD86
IFN-II
FASLG
CD96
PVR
TIGIT
LCK
CD48
IL2

Figure 1: Ancestrally diverse single-cell transcriptome and genomic profiling of uterine carcinosarcoma reflects tumor heterogeneity.

(**A**) Schematic overview of sample collection and tissue-of-origin. Tumor specimens were obtained from uterine carcinosarcoma (UCS) patients. Samples included primary uterine tumors (n = 13) and matched metastatic lesions from ovary and omentum (n = 2). Tissue was collected from anatomically distinct regions including endometrium, ovaries, and omentum. Downstream molecular profiling comprised single-cell RNA sequencing (scRNA-seq, n = 15 specimens) and bulk whole-genome sequencing (WGS, n = 12 specimens).

(**B**) Alluvial plots shows the overall distribution of UCS patients (n = 13) included in this study according to self-reported ethnicity (m) n = 1, mixed ethnicity (MIX) n = 2), body mass index (BMI), and age groups. The BMI groups are classified based on their BMI indices such as Normal >= 18.5 & < 25; Obese class 1 (OC1) >= 25 & < 30; Obese class 2 (OC2) >= 30 & < 40; Obese class 3 (OC3) >= 40.

(**C**) Oncoplot for WGS analysis of 10 primary UCS tumors and 2 matched metastases (Tumor type) showing tumor mutation burden (TMB status), microsatellite instability status (MSI status), and predicted ADMIXTURE-based ancestries.

(**D**) Dimensionality reduction through t-SNE embedding of 97,622 cells derived from 13 primary tumors and 2 matched metastatic lesions (n = 15). Clusters in t-SNE are determined using 50 principal components with a resolution of 2.5.

(**E**) t-SNE plot highlighting lineages of cells identified based on established gene expression markers. Annotated cell lineages include epithelial-like (E-like), mesenchymal-like (M-like), stem-like (Stem), epithelial-to-mesenchymal transition (EMT) states, progenitors, and immune populations.

(**F**) Proportion bar plot shows the distribution of different cell lineages across individual UCS patients. X-axis denotes proportion or percentage of cells contributing to the cell lineages.

Figure 2: UCS cancer cells exhibit high level of heterogeneity, clonality, and cellular plasticity.

(**A**) t-SNE embedding of single-cell transcriptomic data with cell populations classified using CopyKAT-based copy number inference, identifying aneuploid cancer cells, diploid stromal/normal cells, diploid immune cells, and unclassified cells.

(**B**) Heatmap of pairwise Pearson correlations between UCS patients within cancer, stromal, and immune compartments, computed using the top 2,000 most variable genes per component identified by Seurat (VST). Color scale indicates correlation strength (red, positive; black, none; blue, negative).

(**C**) Bar plot showing proportions of cancer cell states per patient, including stem-like (stem-progenitor, mesenchymal stem-like), epithelial (basal, ciliated, luminal), mesenchymal (endothelial, stromal, fibroblast-like), and EMT states.

(**D**) Dot plots of marker gene expression defining stem-like, epithelial-like (E-like), mesenchymal-like (M-like), and EMT states across patients. Color intensity reflects expression level and dot size the fraction of expressing cells. Markers were identified using Seurat ($\log2FC \geq \pm 1$, adjusted $p < 0.05$, Wilcoxon test).

(**E**) UMAP embedding of single-cell data per patient showing annotated cell populations and expression gradients of selected marker genes.

(**F**) UMAP projection of cancer cells highlighting inferred clonal populations ($n = 2$ per patient) based on CopyKAT CNV profiles, with CNV segments clustered using Euclidean distance.

(**G**) Heatmaps showing Pearson correlations between inferred cancer clones and other cellular compartments in representative patients (CS-009, CS-010), illustrating relationships between clonal identities and microenvironmental components.

(**H-I**) UMAP projections of malignant cells from patients CS-009 (**H**) and CS-010 (**I**) with RNA velocity–derived trajectories overlaid on clonal identities. Violin plots show latent time distributions across cell states. Line plots depict gene-specific splicing dynamics along pseudotime (dotted, unspliced; solid, spliced; gray shading, standard deviation).

Figure 3: Trajectory-based analysis reveals molecular adaptations during metastatic progression.

(**A**) Heatmap of top differentially expressed genes ($p < 0.05$, log2FC ±1) between normal endometrium and malignant clones from primary UCS tumors, identified using LIBRA and ranked by Wilcoxon rank-sum test.

(**B**) Bar plots show enriched pathways among upregulated (red) and downregulated (blue) genes in UCS versus normal endometrium. Violin plots display expression of representative genes from TNF-α signaling (*TNFAIP3*, *CXCL2*, *PLAUR*) and EMT (*TWIST1*, *PRRX1*, *FN1*), with significance assessed by Wilcoxon test (ns ≥ 0.05; * < 0.05; ** < 0.01; *** < 0.001; **** < 0.0001).

(**C**) Transcription factor motif enrichment in promoter regions (±250 bp from TSS) of differentially expressed genes ($p < 0.05$, log2FC ±1) in UCS versus normal endometrium. Color (violet–brown) indicates percentage of promoters with enriched motifs; dot size reflects enrichment ratio (MEME).

(**D**) UMAP of single-cell profiles from primary tumor and matched ovarian and omental metastases (CS-011), showing inferred lineage trajectories (left) and latent time progression (right) computed using scVelo.

(**E**) Volcano plot of differential expression between primary tumor and omental metastasis, with significant genes highlighted (log2FC ±1, adjusted $p < 0.05$). Bar plots show enriched pathways for upregulated (red) and downregulated (grey) genes. Analysis performed with LIBRA and GeneSCF.

(**F**) Volcano plot of differential expression between primary tumor and ovarian metastasis with corresponding pathway enrichment (same thresholds and methods as in E).

(**G**) Violin plots of TNF-α signaling (*TNFAIP3*, *CXCL2*, *NFKBIA*) and EMT-related genes (*TWIST1*, *RHOB*, *SAT1*) in UCS versus normal endometrium, highlighting inflammatory and mesenchymal reprogramming. Significance assessed using LIBRA (ns ≥ 0.05; * < 0.05; ** < 0.01; *** < 0.001; **** < 0.0001).

Figure 4: Integrated single-cell profiling reveals immune dysfunction and suppressive remodeling in UCS.

(**A**) UMAP of single-cell transcriptomes highlighting annotated immune populations in UCS tumors, with bar plots showing relative proportions across patients.

(**B**) UMAP of immune populations in normal endometrium (NR) with bar plots showing consistent cell-type proportions across donors, indicating a stable immune landscape compared to UCS.

(**C**) Dot plots of lineage-specific marker expression across T cells ($CD4^+$, $CD8^+$, Tregs), B cells (B, plasma), and myeloid cells (DCs, monocytes, TAMs, mast cells) in UCS tumors. Dot size indicates fraction of expressing cells and color denotes expression level. Markers were identified by Seurat (log2FC $\geq \pm 1$, adjusted $p < 0.05$, Wilcoxon test).

(**D**) Ridge plots showing Treg (*FOXP3*, *IL2RA*) and plasma B cell (*JCHAIN*, *IGHG1*, *IGHG3*, *IGHG4*, *MZB1*) signature scores across UCS tumors, illustrating inter-patient variability.

(**E**) Violin plots (left) show T-cell cytotoxic gene expression in NR and UCS. $CD8^+$ cytotoxicity scores (*PRF1*, *GZMB*) are visualized by distribution and ridge plots (right). Significance assessed by LIBRA (ns ≥ 0.05; * < 0.05; ** < 0.01; *** < 0.001; **** < 0.0001).

(**F**) Violin plots (left) show dysfunction/exhaustion gene expression in NR and UCS. $CD8^+$ dysfunction scores (*PDCD1*, *HAVCR2*, *CTLA4*, *PIK3IP1*) are shown by distribution and ridge plots (right), with significance assessed by LIBRA.

(**G**) Scatter plot shows Spearman correlation between cytotoxic and dysfunction signatures in $CD8^+$ T cells from UCS. Violin plots show expression of tumor-reactive markers (*CXCL13*, *CD39*, *CD103*), highlighting functional heterogeneity.

(**H**) Dot plot of classical NK cell marker expression across lymphocyte populations in UCS and normal tissues, with dot size indicating fraction of expressing cells and color denoting expression level.

(**I**) Violin (left) and ridge plots (right) show expression and distribution of immunosuppressive macrophage signatures (*SPP1*, *FOLR2*, *CD163*, *GPX1*) in UCS versus normal endometrium, highlighting functional shifts. Significance assessed by LIBRA (ns ≥ 0.05; * < 0.05; ** < 0.01; *** < 0.001; **** < 0.0001).

Figure 5: Distinct CAF subpopulations shape the stromal microenvironment in uterine carcinosarcoma.

(**A**) UMAP of stromal fibroblasts from UCS tumors identifying distinct CAF subtypes, including inflammatory CAFs (iCAF), pericyte CAFs (periCAF), and antigen-presenting CAFs (apCAF), defined by marker expression and gating (*PECAM1*$^{-}$, *CD45*$^{-}$, *CD90*$^{+}$).

(**B**) UMAP feature plots showing expression of subtype-defining marker genes across CAF populations, supporting annotation of iCAF, periCAF, and apCAF states.

(**C**) Bar plots of CAF subtype proportions across UCS patients, highlighting interpatient variability in stromal composition.

(**D**) Ridge plots showing CAF signature scores across fibroblasts, including periCAF (*ACTA2*, *NOTCH3*), THBS4^{+} CAF (*THBS4*, *IGF2*), FAP^{+} CAF (*FAP*, *PDGFRA*), iCAF (*CXCR4*, *CCL5*), and apCAF (*CD74*, *HLA-DRA*). The x-axis denotes signature intensity and the y-axis the proportion of cells.

(**E**) Patient-stratified UMAPs showing CAF subtype assignments (categorical colors) with overlaid marker gene expression (gradient), illustrating intra- and interpatient heterogeneity (n = 10).

(**F**) Dot plot summarizing functional gene expression across CAF subtypes (e.g., ECM remodeling, inflammatory signaling, contractility/pericyte programs, antigen presentation). Dot size indicates fraction of expressing cells and color denotes expression level. Markers were identified by Seurat ($\log2FC \geq \pm1$, adjusted $p < 0.05$, Wilcoxon test).

Figure 6: Distinct CAF subpopulations shape the stromal microenvironment in uterine carcinosarcoma.

(**A**) Heatmap showing relative incoming and outgoing ligand–receptor signaling across Cancer, Stromal, and Immune compartments in UCS tumors. Pathways cluster into three compartment-dominant patterns, with top contributors highlighted. Color (blue–red) indicates low-to-high signaling. Significant interactions were identified by permutation testing against randomized cell group labels.

(**B**) Scatter plot of outgoing versus incoming signaling strength across annotated cell types within each compartment. Highly active populations (e.g., $CD8^+$ T cells, vCAFs, FAP^+ CAFs) are highlighted. Signaling strength is defined by network centrality metrics (out-degree/in-degree) identifying dominant senders and receivers.

(**C**) Heatmap of ligand-receptor interactions between high-activity populations ($CD8^+$ T cells, vCAFs, FAP^+ CAFs) and other tumor microenvironment cell types. Color intensity reflects interaction strength; red indicates statistically significant interactions. Interaction probabilities were estimated from ligand–receptor expression across cell types.

(**D**) Protein-protein interaction network of signaling molecules derived from high-activity cell types, clustered using STRING (interaction confidence > 0.9) with the Markov Cluster Algorithm. Enriched modules are associated with immune regulation and exhaustion (PPI enrichment $p < 1.0 \times 10^{-16}$). Nodes represent proteins; edges denote functional/physical interactions, with thickness indicating confidence.

(**E**) Bar plots of cumulative incoming and outgoing signaling strength per pathway across UCS patients, highlighting interpatient variability in tumor microenvironment communication dynamics.